Gravitational form factors and mechanical properties of quarks in protons: A basis light-front quantization approach

Sreeraj Nair[1,*] Chandan Mondal[1,†] Siqi Xu,[1,‡] Xingbo Zhao[1,§] Asmita Mukherjee[2,‖] and James P. Vary[3,¶]

(BLFQ Collaboration)

[1]*Institute for Modern Physics, Chinese Academy of Sciences, Lanzhou-730000, China, School of Nuclear Science and Technology, University of Chinese Academy of Sciences, Beijing 100049, China, and CAS Key Laboratory of High Precision Nuclear Spectroscopy, Institute of Modern Physics, Chinese Academy of Sciences, Lanzhou 730000, China*
[2]*Indian Institute of Technology Bombay, Powai, Mumbai 400076, India*
[3]*Department of Physics and Astronomy, Iowa State University, Ames, Iowa 50011, USA*

We compute the gravitational form factors (GFFs) and study their applications for the description of the mechanical properties such as the pressure, shear force distributions, and the mechanical radius of the proton from its light-front wave functions (LFWFs) based on basis light-front quantization (BLFQ). The LFWFs of the proton are given by the lowest eigenvector of a light-front effective Hamiltonian that incorporates a three-dimensional confining potential and a one-gluon exchange interaction with fixed coupling between the constituent quarks solved in the valence Fock sector. We find acceptable agreement between our BLFQ computations and the lattice QCD for the GFFs. Our *D*-term form factor also agrees well with the extracted data from the deeply virtual Compton scattering experiments at Jefferson Lab, and the results of different phenomenological models. The distributions of pressures and shear forces are similar to those from different models.

I. INTRODUCTION

Nucleons are confined systems of partons (quarks and gluons) with pressure and energy inside, dictated by the strong interaction. However, understanding the color confinement and the mass generation of the nucleon in quantum chromodynamics (QCD) theory remains one of the central questions in modern particle and nuclear physics. As a composite system, various distribution functions, such as form factors, parton distribution functions (PDFs), generalized parton distributions (GPDs), transverse momentum dependent parton distributions (TMDs), etc., are often used to describe the structure of the nucleon. The form factors of the nucleon give critical information about many fundamental aspects of its structure. The charge and magnetization distributions are encoded in the electromagnetic form factors [1,2], while the mechanical properties of the nucleon, namely the mass, spin, pressure, and shear force are well encoded in the gravitational form factors (GFFs) [3–6]. Specifically, one can gain a deeper knowledge on how the nucleon is mechanically shaped by its partons by studying the Druck term (*D*-term) GFFs [5]. The GFFs are parametrized as the matrix elements of the energy-momentum tensor (EMT) in the nucleon states. The components of the EMT provide how matter interacts to the gravitational field. Thus these form factors can be extracted by direct measurement of the interaction of the nucleon with a strong gravitational field such as a neutron star. However, due to weak gravitational interaction, the direct access to them experimentally is very difficult. An indirect way to extract the GFFs experimentally is from hard exclusive processes, for example, deeply virtual Compton scattering (DVCS) and deeply-virtual meson production (DVMP), which are sensitive to GPDs. The GFFs are defined as the second Mellin moments of the GPDs. The quark GPDs in the nucleon have been constrained in limited

[*]Contact author: sreeraj@impcas.ac.cn
[†]Contact author: mondal@impcas.ac.cn
[‡]Contact author: xsq234@impcas.ac.cn
[§]Contact author: xbzhao@impcas.ac.cn
[‖]Contact author: asmita@phy.iitb.ac.in
[¶]Contact author: jvary@iastate.edu

kinematic regions by DVCS and DVMP experiments at JLab [7–9], COMPASS [10], HERA [11–13], and HERMES [14]. The world datasets have been summarized in Refs. [15–17]. Ongoing investigations at COMPASS and within the 12 GeV program at JLab will significantly improve accesses to these quantities. The first extraction of the quark D-term form factors from DVCS and the pressure distribution inside the proton was reported in Ref. [5]. However, the DVCS is nearly insensitive to the gluon and thus, the gluon D-term form factor is rarely extracted. The gluon contributions to the nucleon D-term form factor will be accessed at the future high-luminosity electron-ion colliders (EICs) [18,19].

The nucleon matrix element of the EMT involves four GFFs, namely $A(Q^2)$, $B(Q^2)$, $D(Q^2)$, and $\bar{C}(Q^2)$, where Q^2 is the squared momentum transfer from the initial to final nucleon. They encode information on the distributions of energy density, angular momentum, and internal forces in the interior of the nucleon. The GFFs A and B are linked to the mass and spin of the nucleon. The Ji's sum rule [20] relates them to the partonic contribution to the total angular momentum J. They are again related to the generators of the Poincaré group, which provides constraints on them at $Q^2 = 0$, which facilitates accessing these form factors from the experimental data. The form factor $D(Q^2)$ is related to the basic mechanical properties of the nucleon such as the pressure and stress distributions [3–6]. It contributes to the DVCS process when there is nonzero momentum transfer in the longitudinal direction. By virtue of energy momentum conservation, the form factor $\bar{C}(Q^2)$ contributes to both the quark and gluon parts with the same magnitude but with opposite signs, therefore $\sum_{i=q,g} \bar{C}_i(Q^2) = 0$. This form factor records the reshuffling of forces between the quark and gluon subsystems inside the nucleon [21].

There has been significant progress in the theoretical determination of the nucleon GFFs, in particular through phenomenology, QCD inspired models, and lattice QCD. The GFFs of the nucleon have been studied via chiral perturbation theory [22–24], chiral quark soliton model [25–29], bag model [30], Skyrme model [31,32], light cone QCD sum rules at leading order [33], light-front quark-diquark model motivated by AdS/QCD [34–38], dispersion relation [39], instanton picture [21], instant and front form [4], holographic QCD [40–43], lattice QCD [44–49], strongly coupled scalar theory [50], etc., while the asymptotic behavior of the GFFs has been reported in Refs. [51,52]. On the other hand, the gluon contributions to the nucleon GFFs are far less well-constrained and have so far only been investigated in holographic light-front QCD framework [53], dressed quark model [54] and lattice QCD [55–60]. To date, no experimental constraints on gluon GFFs of the nucleon have been achieved. However, they are accessible via photo/leptoproduction of J/ψ and Υ [61–63]; J/ψ production is investigated in experiments, which are ongoing

at JLab [64], whereas Υ production are proposed at the upcoming EICs [18,19]. The quark GFFs for the nucleon have been extracted at JLab from DVCS [5] and the constraints on the quark GFFs can be further improved via the GPDs accessible at several existing and upcoming experimental facilities, which include the PANDA experiment at the Facility for Antiproton and Ion Research [65], the proposed EICs [18,19], the nuclotron-based ion collider facility [66], the International Linear Collider, and the Japan proton accelerator complex [67].

Our theoretical framework to study the nucleon properties is based on basis light-front quantization (BLFQ) [68], which provides a Hamiltonian formalism for solving the relativistic many-body bound state problem in quantum field theories [69–86]. In this paper, we compute the quark GFFs of the proton and investigate their applications for the description of the mechanical properties, i.e., the distributions of pressures and shear forces inside the proton from its light-front wave functions (LFWFs) based on the BLFQ with only the valence Fock sector of the proton considered. The LFWFs feature all three active quarks' flavor, spin, and three-dimensional spatial information on the same footing. Our effective Hamiltonian incorporates a three-dimensional confinement potential embodying the light-front holography in the transverse direction [87] and a complimentary longitudinal confinement [72]. The Hamiltonian also includes a one-gluon exchange interaction with fixed coupling to account for the spin structure [78]. The nonperturbative solutions for the three-body LFWFs generated by the recent BLFQ study of the nucleon [79] have been applied successfully to generate the electromagnetic and axial form factors, radii, PDFs, GPDs, TMDs, and many other properties of the nucleon [78,79,88–92]. Here, we extend those studies to calculate the proton GFFs and their application for the description of the mechanical properties.

The rest of the paper is organized as follows. In Sec. II, we briefly summarize the BLFQ framework for the nucleon. The proton GFFs are evaluated within BLFQ and discussed in Sec. III. We present the numerical results for the GFFs and explore the mechanical properties of proton, e.g., the pressures, energy density distributions, shear forces, and the mechanical radius in Sec. IV. At the end, we provide a brief summary and conclusions in Sec. V.

II. PROTON WAVE FUNCTION FROM BASIS LIGHT-FRONT QUANTIZATION

The LFWFs encoding the structural information of hadronic bound states are achieved as the eigenfunctions of the eigenvalue problem of the Hamiltonian, $H_{\mathrm{LF}}|\Psi\rangle = M_{\mathrm{h}}^2|\Psi\rangle$, with H_{LF} and M_{h}^2 being the light-front Hamiltonian and the mass square eigenvalue of the hadron, respectively. The light-front effective Hamiltonian for the proton with quarks being the only explicit degree of freedom is given by [78]

$$H_{\text{eff}} = \sum_a \frac{\vec{k}_{\perp a}^2 + m_a^2}{x_a} + \frac{1}{2}\sum_{a\neq b}\kappa^4\left[x_a x_b(\vec{r}_{\perp a} - \vec{r}_{\perp b})^2 - \frac{\partial_{x_a}(x_a x_b \partial_{x_b})}{(m_a + m_b)^2}\right]$$

$$+ \frac{1}{2}\sum_{a\neq b}\frac{F_C 4\pi\alpha_s}{Q_{ab}^2}\bar{u}(k_a', s_a')\gamma^\mu u(k_a, s_a)\bar{u}(k_b', s_b')\gamma^\nu u(k_b, s_b)g_{\mu\nu}, \quad (1)$$

where $\vec{k}_{\perp a}$ and x_a represent the relative transverse momentum and the longitudinal momentum fraction carried by quark a. m_a defines the mass of the quark a, and κ is the strength of the confining potential. The variable $\vec{r}_\perp = \vec{r}_{\perp a} - \vec{r}_{\perp b}$ represents the transverse distance between two quarks. The last term in the Hamiltonian indicates the one-gluon exchange interaction with $Q_{ab}^2 = -q^2 = -(1/2)(k_a' - k_a)^2 - (1/2)(k_b' - k_b)^2$ being the average momentum transfer squared and $F_C = -2/3$ is the color factor; α_s is the coupling constant; and $g_{\mu\nu}$ refers to the metric tensor. $u(k_a, s_a)$ corresponds to the spinor with momentum k_a and spin s_a.

In the BLFQ approach, the discretized plane-wave basis is conveniently adopted in the longitudinal direction, whereas we utilize the 2D harmonic oscillator (HO) function for the transverse direction [68,69]. Solving the eigenvalue equation of the Hamiltonian, Eq. (1), in the chosen basis space provides the eigenvalues as squares of the system masses, and the eigenfunctions that describe the LFWFs. The lowest eigenfunction with the relevant symmetries is naturally specified as the proton state. The LFWFs of the proton are expressed in terms of the basis function as

$$\Psi^\Lambda_{\{x_i, \vec{k}_{i\perp}, \lambda_i\}} = \sum_{\{n_i, m_i\}}\psi^\Lambda_{\{x_i, n_i, m_i, \lambda_i\}}\prod_i\phi_{n_i, m_i}(\vec{k}_{i\perp}; b), \quad (2)$$

with $\psi^\Lambda_{\{x_i, n_i, m_i, \lambda_i\}} = \langle P, \Lambda|\{x_i, n_i, m_i, \lambda_i\}\rangle$ representing the LFWF in the BLFQ basis obtained by diagonalizing Eq. (1) numerically, where $|P, \Lambda\rangle$ defines the proton state with P and Λ being the momentum and the helicity of the state. The 2D-HO function we employ as the transverse basis function is given by

$$\phi_{n,m}(\vec{k}_\perp; b) = \frac{\sqrt{2}}{b(2\pi)^{\frac{3}{2}}}\sqrt{\frac{n!}{(n+|m|)!}}e^{-\vec{k}_\perp^2/(2b^2)}\left(\frac{|\vec{k}_\perp|}{b}\right)^{|m|}$$

$$\times L_n^{|m|}\left(\frac{\vec{k}_\perp^2}{b^2}\right)e^{im\theta}, \quad (3)$$

where b defines its scale parameter; n and m correspond to the principal and orbital quantum numbers, respectively, and $L_n^{|m|}$ is the associated Laguerre polynomial. The transverse basis truncation is designated by the dimensionless cutoff parameter N_{max}, such that $\sum_i(2n_i + |m_i| + 1) \leq N_{\text{max}}$. The basis truncation N_{max} plays implicitly the role of the infrared

(IR) and ultraviolet (UV) regulators for the LFWFs in the transverse direction, with an IR cutoff $\Lambda_{\text{IR}} \approx b/\sqrt{N_{\text{max}}}$ and a UV cutoff $\Lambda_{\text{UV}} \approx b\sqrt{N_{\text{max}}}$. In the discretized plane-wave basis, the longitudinal momentum fraction x_i of the Fock particles is defined as $x_i = p_i^+/P^+ = k_i/K$, with the dimensionless quantity $K = \sum_i k_i$, where $k = \frac{1}{2}, \frac{3}{2}, \frac{5}{2}, \ldots$ signifies the choice of antiperiodic boundary conditions. The longitudinal basis cutoff K controls the numerical resolution and regulates the longitudinal direction. The multiparticle basis states have the total angular momentum projection $M_J = \sum_i(m_i + \lambda_i)$, where λ denotes the quark helicity.

The parameters in the effective Hamiltonian are determined to reproduce the nucleon mass and its electromagnetic properties [79]. The model LFWFs have demonstrated significant effectiveness in analyzing a broad range of nucleon properties, including electromagnetic and axial form factors, radii, PDFs, quark helicity asymmetries, GPDs, TMDs, and angular momentum distributions, achieving notable success across various metrics. [78,79,90].

III. GRAVITATIONAL FORM FACTORS

The gauge invariant symmetric form of the QCD EMT is given by [93]

$$\theta^{\mu\nu} = \frac{1}{2}\bar{\psi}i[\gamma^\mu D^\nu + \gamma^\nu D^\mu]\psi - F^{\mu\lambda a}F^\nu_{\lambda a} + \frac{1}{4}g^{\mu\nu}(F_{\lambda\sigma a})^2$$

$$- g^{\mu\nu}\bar{\psi}(i\gamma^\lambda D_\lambda - m)\psi, \quad (4)$$

with ψ and A^μ being the fermion and boson fields, respectively. $F_a^{\mu\nu}$ is the field strength tensor for non-Abelian gauge theory, which is expressed as

$$F_a^{\mu\nu} = \partial^\mu A_a^\nu - \partial^\nu A_a^\mu + gf^{abc}A_b^\mu A_c^\nu, \quad (5)$$

where the covariant derivative $iD^\mu = i\overset{\leftrightarrow}{\partial}{}^\mu + gA^\mu$ such that $\alpha(i\overset{\leftrightarrow}{\partial}{}^\mu)\beta = \frac{i}{2}\alpha(\partial^\mu\beta) - \frac{i}{2}(\partial^\mu\alpha)\beta$. In this work, we focus only on the fermionic part of the EMT given in Eq. (4). Note that the last term in Eq. (4) vanishes owing to the equation of motion and thus, we have the following fermionic contribution to the EMT:

$$\theta_{\mathsf{q}}^{\mu\nu} = \frac{1}{2}\bar{\psi}i[\gamma^\mu D^\nu + \gamma^\nu D^\mu]\psi. \quad (6)$$

The matrix elements of local operators such as electromagnetic current and EMT have a precise representation using LFWFs of bound systems such as hadrons. The GFFs are linked to the matrix elements of the EMT, $\theta^{\mu\nu}$, whereas the second Mellin moment of the GPDs also gives the GFFs. For a spin-$1/2$ composite system, the standard parametrization of the symmetric EMT $\theta^{\mu\nu}$ involving the GFFs reads [94,95]

$$
\begin{aligned}
\langle P', \Lambda' | \theta_i^{\mu\nu}(0) | P, \Lambda \rangle = \bar{u}(P', \Lambda') \Bigg[&-B_i(Q^2) \frac{\bar{P}^\mu \bar{P}^\nu}{M} + (A_i(Q^2) \\
&+ B_i(Q^2)) \frac{1}{2} (\gamma^\mu \bar{P}^\nu + \gamma^\nu \bar{P}^\mu) \\
&+ C_i(Q^2) \frac{q^\mu q^\nu - q^2 g^{\mu\nu}}{M} \\
&+ \bar{C}_i(Q^2) M g^{\mu\nu} \Bigg] u(P, \Lambda),
\end{aligned}
\tag{7}
$$

where $\bar{u}(P', \Lambda')$, $u(P, \Lambda)$ are the Dirac spinors and $\bar{P}^\mu = \frac{1}{2}(P' + P)^\mu$ is the average four momentum of the system. M is the mass of the system and $\Lambda(\Lambda')$ is the helicity of the initial (final) state of the system such that $(\Lambda, \Lambda') \equiv \{\uparrow, \downarrow\}$. Here $\uparrow(\downarrow)$ represents the positive (negative) spin projection along the z-axis. The Lorentz index $(\mu, \nu) \equiv \{+, -, 1, 2\}$. $Q^2 = -q^2$ is the square of the momentum transfer. We consider the symmetric Drell-Yan frame such that the longitudinal momentum transfer $q^+ = 0$ and the average transverse momentum $\bar{P}^\perp = 0$. The form factors $A_q(Q^2)$ and $B_q(Q^2)$ are extracted form the θ_q^{++} component of the EMT. In light-front dynamics the conserved Noether current associated with the conserved 4-momentum is $\theta_q^{+\mu}$ [96]. Furthermore, the operator θ_q^{++} removes a quark (or antiquark) possessing momentum k' (or k) and spin projection λ along the z-axis, and then generates a quark (or antiquark) with identical spin and momentum k' (or k) [97]. The GFF $A_q(Q^2)$ is analogous to the Dirac form factor since it is obtained by summing over the helicity conserving states, whereas $B_q(Q^2)$, which is obtained by summing over the helicity flip states, is analogous to the Pauli form factor. The GFFs $C_q(Q^2)$ and $\bar{C}_q(Q^2)$ are extracted from the θ_q^{jk} transverse component of the EMT such that $(j, k) \equiv (1, 2)$. We compactly express the matrix elements of the EMT required to extract the four GFFs as

$$
\mathcal{M}_{\Lambda\Lambda'}^{\mu\nu} = \frac{1}{2} [\langle P', \Lambda' | \theta_q^{\mu\nu}(0) | P, \Lambda \rangle],
\tag{8}
$$

where the proton state with momentum P and helicity Λ within the valence Fock sector can be written in terms of three-particle LFWFs,

$$
\begin{aligned}
|P, \Lambda\rangle = \int \prod_{i=1}^3 \Bigg[\frac{dx_i d^2\vec{k}_{i\perp}}{\sqrt{x} 16\pi^3} \Bigg] 16\pi^3 \delta \Bigg(1 - \sum_{i=1}^3 x_i \Bigg) \delta^2 \\
\times \Bigg(\sum_{i=1}^3 \vec{k}_{i\perp} \Bigg) \Psi_{\{x_i, \vec{k}_{i\perp}, \lambda_i\}}^\Lambda | \{x_i P^+, \vec{k}_{i\perp} + x_i \vec{P}_\perp, \lambda_i\} \rangle.
\end{aligned}
\tag{9}
$$

The GFFs $A_q(Q^2)$ and $B_q(Q^2)$ can then be obtained using Eq. (8) as follows:

$$
\mathcal{M}_{\uparrow\uparrow}^{++} + \mathcal{M}_{\downarrow\downarrow}^{++} = 2(P^+)^2 A_q(Q^2),
\tag{10}
$$

$$
\mathcal{M}_{\uparrow\downarrow}^{++} + \mathcal{M}_{\downarrow\uparrow}^{++} = \frac{iq^{(2)}}{M} (P^+)^2 B_q(Q^2),
\tag{11}
$$

while the GFF $C_q(Q^2)$ is computed from the transverse components using

$$
\mathcal{M}_{\uparrow\uparrow}^{12} + \mathcal{M}_{\downarrow\downarrow}^{12} = 4 C_q(Q^2) q^{(1)} q^{(2)}.
\tag{12}
$$

The GFF $\bar{C}_q(Q^2)$ can be computed from the nonconservation of the partial EMT [4] which gives us

$$
q_\mu \mathcal{M}_{\uparrow\downarrow}^{\mu\nu} = \bar{C}_q(Q^2) q^\nu M \left(-q^{(1)} - iq^{(2)} \right).
\tag{13}
$$

The GFFs $A_q(Q^2)$ and $B_q(Q^2)$ can be written in terms of the overlap of LFWFs upon substituting the proton valence Fock state as shown in Eq. (9) into the matrix element of the energy-momentum tensor in Eq. (8) and we get the following expression:

$$
\begin{aligned}
A_q(Q^2) &= \frac{1}{2} \sum_{\{\lambda_i\}} \int [d\mathcal{X} d\mathcal{P}_\perp] x_1 \Bigg\{ \Psi_{\{x_i', \vec{k}_{i\perp}', \lambda_i\}}^{\uparrow *} \Psi_{\{x_i, \vec{k}_{i\perp}, \lambda_i\}}^{\uparrow} + \Psi_{\{x_i', \vec{k}_{i\perp}', \lambda_i\}}^{\downarrow *} \Psi_{\{x_i, \vec{k}_{i\perp}, \lambda_i\}}^{\downarrow} \Bigg\}, \\
iq^{(2)} B_q(Q^2) &= M \sum_{\{\lambda_i\}} \int [d\mathcal{X} d\mathcal{P}_\perp] x_1 \Bigg\{ \Psi_{\{x_i', \vec{k}_{i\perp}', \lambda_i\}}^{\uparrow *} \Psi_{\{x_i, \vec{k}_{i\perp}, \lambda_i\}}^{\downarrow} + \Psi_{\{x_i', \vec{k}_{i\perp}', \lambda_i\}}^{\downarrow *} \Psi_{\{x_i, \vec{k}_{i\perp}, \lambda_i\}}^{\uparrow} \Bigg\},
\end{aligned}
\tag{14}
$$

where the longitudinal and transverse momenta of the struck quark are $x'_1 = x_1$ and $k'_{1\perp} = k_{1\perp} + (1 - x_1)q_\perp$ respectively. The spectator momenta are $x'_i = x_i$ and $k'_{i\perp} = k_{i\perp} + x_i q_\perp$ with $i = (2, 3)$. The shorthand notation used for the integration measure is as follows:

$$[\mathrm{d}\mathcal{X}\mathrm{d}\mathcal{P}_\perp] \equiv \prod_{i=1}^{3}\left[\frac{\mathrm{d}x_i \mathrm{d}^2 k_{i\perp}}{16\pi^3}\right]16\pi^3\delta\left(1 - \sum_{i=1}^{3}x_i\right)$$
$$\times \delta^2\left(\sum_{i=1}^{3}k_{i\perp}\right). \tag{15}$$

TABLE I. Parameters of the model with a transverse basis truncation set at $N_{\max} = 10$ and a longitudinal truncation at $K = 16.5$.

$m_{q/k}$	$m_{q/g}$	κ	α_s
0.3 GeV	0.2 GeV	0.34 GeV	1.1 ± 0.1

Similarly the expression for $C_q(Q^2)$ and $\bar{C}_q(Q^2)$ can be extracted from the equations below,

$$q^{(1)}q^{(2)}C_q(Q^2) = \frac{1}{8}\sum_{\{\lambda_i\}}\int[\mathrm{d}\mathcal{X}\mathrm{d}\mathcal{P}_\perp]\mathcal{O}^1\mathcal{O}^2\left\{\Psi^{\uparrow *}_{\{x'_i, \vec{k}'_{i\perp}, \lambda_i\}}\Psi^{\uparrow}_{\{x_i, \vec{k}_{i\perp}, \lambda_i\}} + \Psi^{\downarrow *}_{\{x'_i, \vec{k}'_{i\perp}, \lambda_i\}}\Psi^{\downarrow}_{\{x_i, \vec{k}_{i\perp}, \lambda_i\}}\right\},$$

$$\left(-q^{(1)} - iq^{(2)}\right)q^{(1)}\bar{C}_q(Q^2) = -\frac{1}{M}\sum_{\{\lambda_i\}}\int[\mathrm{d}\mathcal{X}\mathrm{d}\mathcal{P}_\perp](q^{(1)}\mathcal{O}^1\mathcal{O}^1 + q^{(2)}\mathcal{O}^2\mathcal{O}^1)\left\{\Psi^{\downarrow *}_{\{x'_i, \vec{k}'_{i\perp}, \lambda_i\}}\Psi^{\uparrow}_{\{x_i, \vec{k}_{i\perp}, \lambda_i\}}\right\}, \tag{16}$$

where the operator $\mathcal{O}^j = 2k_\perp^{(j)} + (1 - x)q_\perp^{(j)}$. Identities relating the overlap of HO wave function pertaining to the calculation of Eq. (16) is shown in Appendix B. The LFWF with negative helicity ($\Lambda = \downarrow$) is obtained from the wavefunction with positive helicity ($\Lambda = \uparrow$) using the mirror parity symmetry [98] which gives the following relation:

$$\psi^{\downarrow}_{\{x_i, n_i, m_i, \lambda_i\}} = (-1)^{\sum_i m_i + 1}\psi^{\uparrow}_{\{x_i, n_i, -m_i, -\lambda_i\}}. \tag{17}$$

IV. NUMERICAL RESULTS

In our calculations, the quark mass influences both the kinetic energy and the one-gluon exchange interaction (OGE) terms. We opted for different quark mass values in these terms due to the distinct physics they represent. Specifically, the kinetic mass term captures long-distance physics, while the OGE term encapsulates short-distance physics through the derived interaction arising from single-gluon exchanges between quarks. This effective OGE compensates for fluctuations spanning from the valence Fock sector to higher Fock sectors.

We now outline our reasoning for the flexibility in choosing the vertex mass. Specifically, our approach incorporates an effective OGE interaction that connects short-distance physics and approximately describes processes where valence quarks emit and absorb a gluon, causing the system to fluctuate between the $|qqq\rangle$, $|qqqg\rangle$, and higher Fock sectors. In the intuitive picture of mass evolution in renormalization group theory, the dynamical OGE also contributes to the quark mass from higher momentum scales, leading to a decrease in quark mass due to gluon dynamics. Consequently, it is suggested that

the mass in the OGE interaction would be lighter than the kinetic mass, which is associated with long-range physics in our effective Hamiltonian. Therefore, the quark mass in the OGE has been introduced as an independent phenomenological parameter in our effective Hamiltonian. Alongside other parameters, it successfully describes a wide class of proton observables, e.g., the electromagnetic and axial form factors, radii, PDFs, helicity asymmetries, TMDs, etc., with remarkable overall success [78,79,88,89,91,99]. This treatment is also acknowledged and adopted in the literature [100–102]. Besides the quark mass, the model includes two additional parameters; the confinement potential strength (κ) and the coupling constant (α_s), both listed in Table I. Our results employ truncation parameters with values $N_{\max} = 10$ and $K = 16.5$. We calibrated these parameters against existing experimental data on the Dirac and Pauli form factors [79]. Using this setup, we derive the proton's four gravitational form factors of the symmetric energy-momentum tensor and depict the mechanical properties, including the quark pressure and shear distributions inside the proton.

In Fig. 1, we present our calculations for the GFFs $A(Q^2)$ and $B(Q^2)$, along with predictions from lattice QCD [103]. The contributions from the u quark and d quark are individually presented for both $A(Q^2)$ and $B(Q^2)$ at both the initial and final scales. As the existing lattice data is at a higher scale of $\mu^2 = 4$ GeV^2, we have evolved our results for a consistent comparison. For the scale evolution, we employed the Dokshitzer-Gribov-Lipatov-Altarelli-Parisi (DGLAP) equations of QCD [104–106], specifically utilizing the next-to-next-to-leading order (NNLO) variant. The evolution is done at each value of Q^2 for the GPDs $xH^q(x, Q^2)$ and $xE^q(x, Q^2)$ as their
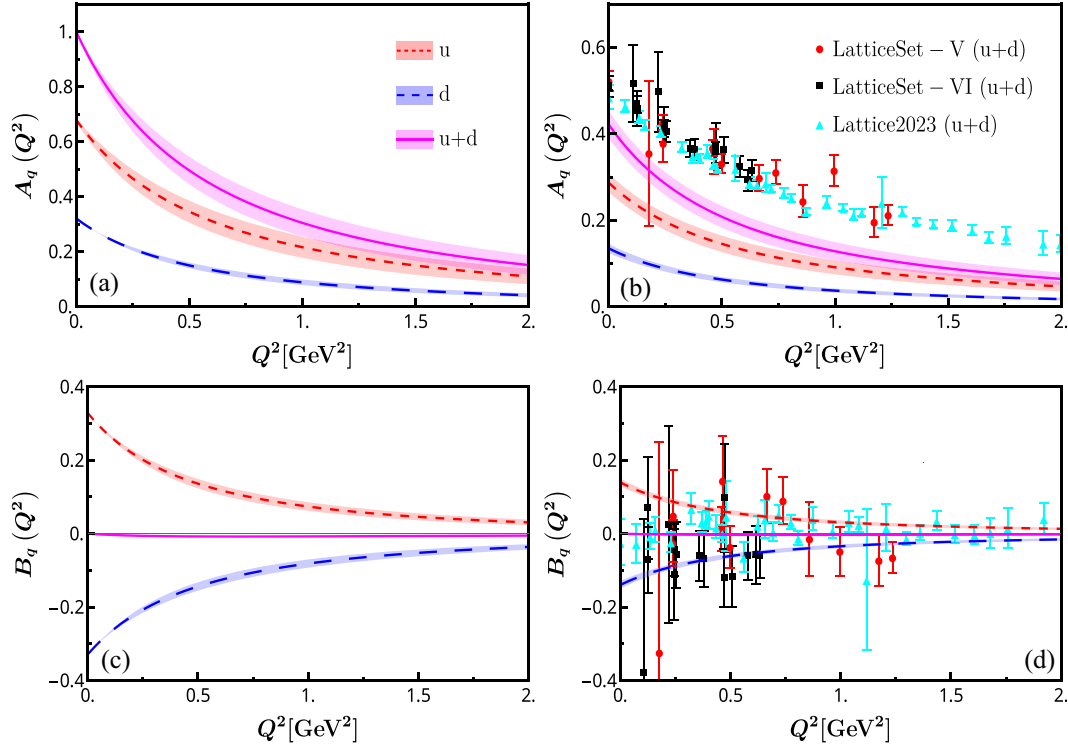
FIG. 1. Plots illustrating GFFs for both $A_q(Q^2)$ and $B_q(Q^2)$ at two scales, plotted against Q^2. These include: (a) $A_q(Q^2)$ at an initial scale $\mu_0^2 = 0.195 \pm 0.020$ GeV^2, (b) $A_q(Q^2)$ evolved to $\mu^2 = 4$ GeV^2, (c) $B_q(Q^2)$ at the same initial scale, and (d) $B_q(Q^2)$ evolved to $\mu^2 = 4$ GeV^2. In the plots, solid magenta lines with shaded areas signify combined u and d quark contributions, while individual d and u quark contributions are shown with dashed blue and red lines, respectively. The shaded areas represent uncertainties: 10% in the α_s coupling at the initial scale and a combined 10% in μ_0^2 and α_s at the evolved scale, calculated in quadrature. The evolved GFFs are compared against lattice data at $\mu^2 = 4$ GeV^2, shown as red circles and black squares from Ref. [103], and cyan triangles from Ref. [109].

moments correspond to the GFFs $A(Q^2)$ and $B(Q^2)$ respectively. The GFFs were evolved from an initial scale of $\mu_0^2 = 0.195 \pm 0.020$ GeV^2 to the lattice scale using the higher order perturbative parton evolution toolkit [107]. The initial scale is chosen so as to match the moment of the valence quark PDFs [79]. The model scale is determined by matching the moment of the valence quark PDFs, $\langle x \rangle_q = \int_0^1 dx \, x f_1^q(x)$, at $\mu^2 = 10$ GeV^2 with the results from global fits after performing QCD evolution of our valence quark PDFs. We use the NNLO DGLAP equations of QCD to evolve our valence quark PDFs from our model scale μ_0^2 to a higher scale μ^2. While applying the DGLAP equations numerically from such a low scale, we ensure that the running coupling $\alpha_s(\mu^2)$ saturates in the infrared at a maximum cutoff value of $\alpha_s \sim 1$, consistent with our fit value [79]. Our analyses indicate that at the initial scale, the values for $A^{u+d}(0)$ and $B^{u+d}(0)$ are 1 and 0, respectively. This is expected as a consequence of the conservation of momentum and total angular momentum. The physical meaning of $A_q(0)$ is the momentum fraction carried by quarks inside the proton. Our model Hamiltonian includes only quark degrees of freedom,

resulting in $A^{u+d}(0) = 1$, indicating that the quarks carry all the proton's momentum in our quark-only model. So, at the initial model scale, we have $A_q^u(0) + A_q^d(0) = 1$. However, scale evolution incorporates contributions from gluons and sea quarks, which are absent in the initial quark-only model. After evolution, $1 - A(0)$ represents the momentum carried by gluons and sea quarks, dynamically generated through the evolution process. The value of $B^{u+d}(0) = 0$ is referred to as the vanishing of the total anomalous gravitomagnetic moment [108]. We find that $A^u > A^d$ and B^u is positive while B^d is negative. Following the evolution process, the magnitudes of both functions exhibit a decline. We find that the lattice results for $A^{u+d}(Q^2)$ significantly exceed our evolved result at $\mu^2 = 4$ GeV^2 especially at higher Q^2.

In Fig. 2, the D-term form factor and the GFF $\bar{C}(Q^2)$ are depicted. Panels (a) and (b) of Fig. 2 display our findings for $D(Q^2)$ at the initial and evolved final scales, respectively. The D-term for both d and u quarks is observed to be negative, with the magnitude being larger for the u quark. Following scale evolution, the characteristics of our D-term, as shown in Fig. 2(b), correspond well with the
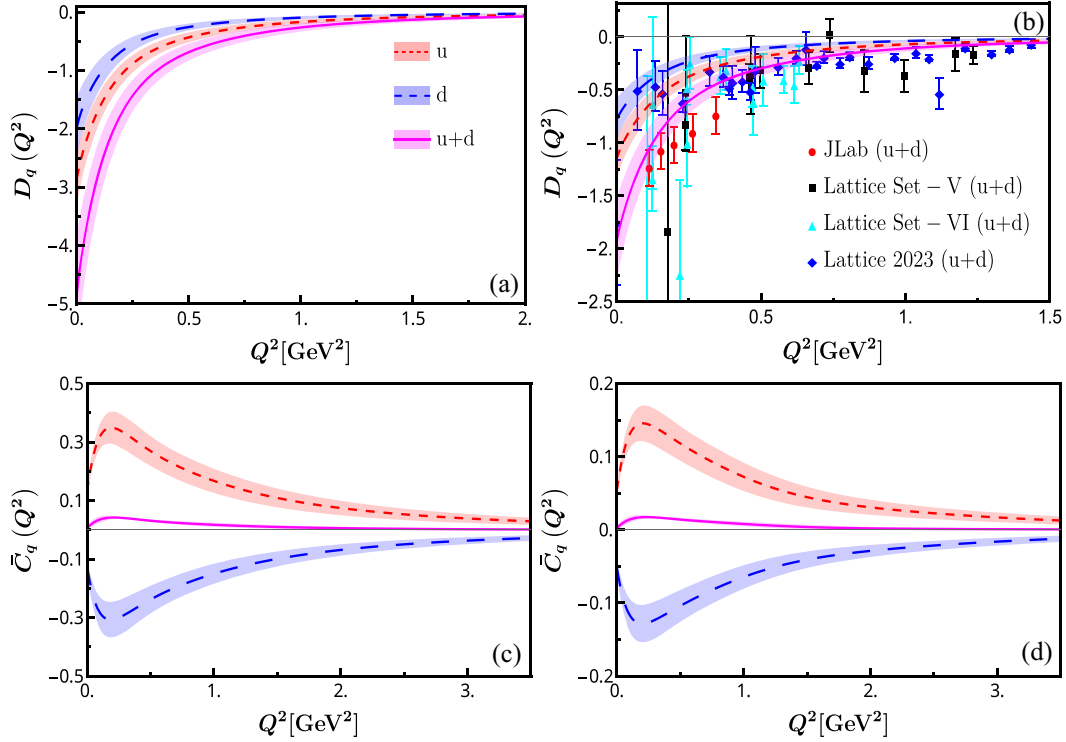
FIG. 2. Plots illustrating GFFs for both $D_q(Q^2)$ and $\bar{C}_q(Q^2)$ across different scales: (a) $D_q(Q^2)$ at an initial scale of $\mu_0^2 = 0.195 \pm 0.020$ GeV^2, (b) $D_q(Q^2)$ at a final evolved scale of $\mu^2 = 4$ GeV^2, (c) $\bar{C}_q(Q^2)$ at the initial scale, and (d) $\bar{C}_q(Q^2)$ at the final evolved scale, all versus Q^2. The solid magenta lines with bands in each plot denote the combined contributions of the u and d quarks, while the dashed blue and red lines represent individual contributions from the d and u quarks, respectively. The bands across the plots at the initial scale signify a 10% uncertainty in the α_s coupling constant whereas the bands across the evolved results are due to 10% uncertainty in μ_0^2 and the coupling constant α_s. In plot (b) the red circles are the data points taken from [6] where they have rescaled the Jefferson Lab experimental data used in [5] to $\mu^2 = 4$ GeV^2. Lattice data are represented by cyan triangles and black squares [103]. Additionally, the evolved $D_q^{u+d}(Q^2)$ results are compared with lattice data at $\mu^2 = 4$ GeV^2 as depicted by blue diamond from Ref. [109].

lattice results [103,109] and JLab experimental data [5].[1] A negative D-term is indicative of a stable bound system, and our evolved results for the D-term show a reasonable alignment with the JLab data at $\mu^2 = 4$ GeV^2.

The D-term, related to the stress tensor T^{ij}, provides insight into the distribution of internal forces within the nucleon, a subtlety not as readily apparent as the well-studied mass and spin properties [110]. Its calculation involves the transverse components of the EMT operator, as evident from Eq. (12). This introduces a coupling between the ψ^+ and ψ^- quark fields, where, in the light cone gauge, the ψ^- field can be expressed in terms of the ψ^+ field due to constraints imposed by the corresponding equation of motion. Furthermore, the involvement of constraint equations implies the potential for nondiagonal contributions arising from overlaps of light-front wave-functions originating from Fock sectors with differing numbers of partons. A more comprehensive calculation

of the D-term would therefore necessitate considering contributions from nondiagonal overlaps resulting from the inclusion of higher Fock sectors. However, it is important to note that the focus of our current work was to highlight the quark contribution from the valence Fock sector.

Panels (c) and (d) of Fig. 2 present the $\bar{C}(Q^2)$ form factor following our BLFQ framework. We observe $\bar{C}^u(Q^2) > 0$ and $\bar{C}^d(Q^2) < 0$, with the aggregate $\bar{C}^{u+d}(Q^2)$ remaining near zero for most Q^2 values. According to the sum rule, the total $\bar{C}^{u+d}(Q^2)$ should equal zero for all values of Q^2. Within our BLFQ approach, focusing on the valence Fock sector of the proton state, this condition is partially met, with $\bar{C}^{u+d}(0)$ being 0.0063 at the initial scale and 0.0024 at the evolved scale of $\mu^2 = 4$ GeV^2. It should be emphasized that the $\bar{C}_q$ form factors calculated in this work represent solely the contributions from the quark in the valence Fock sector of the proton. Accurately computing the genuine $\bar{C}_q$ form factors requires considering contributions from the gluon sector, since the flavor-decomposed $\bar{C}_q$ form factors are intrinsically linked to the twist-4 GPDs [111].

---

[1]The notation for the D-term used in [5] is $d_q(Q^2) = \frac{4}{5}D_q(Q^2)$ and have $\mu^2 = 1.4$ GeV^2.

TABLE II. The GFFs for the valence quark combination at $Q^2 = 0$ are compared with predictions from other models and data from JLab. Predictions from the Skyrme and χQSM models take into account contributions from both quarks and gluons and are not dependent on scale. The notation $(\mu_0 \to \mu)$ indicates the evolution from the starting scale μ_0 to the final scale μ.

Approaches/models	$A_q^{u+d}(0)$	$J_q(0) = \frac{1}{2}[A_q^{u+d}(0) + B_q^{u+d}(0)]$	$D^{u+d}(0) = 4C^{u+d}(0)$	$\bar{C}_q^{u+d}(0)$
This work ($\sqrt{0.195} \to 2$ GeV)	0.420 ± 0.032	0.210 ± 0.016	-1.925 ± 0.398	0.0024 ± 0.0034
LQCD (2 GeV) [44]	0.675	0.34	$\cdots$	$\cdots$
LQCD (2 GeV) [45]	0.547	0.33	-0.80	$\cdots$
LQCD (2 GeV) [46]	0.553	0.238	-1.02	$\cdots$
LQCD (2 GeV) [103]	0.520	0.213	-1.07	$\cdots$
LQCD (2 GeV) [48]	0.572	0.226	$\cdots$	$\cdots$
LQCD (2 GeV) [49]	0.565	0.314	$\cdots$	$\cdots$
χPT (2 GeV) [24]	0.538	0.24	-1.44	$\cdots$
IFF (2 GeV) [4]	0.55	0.24	-1.28	-0.11
Asymptotic (∞GeV) [51]	$\cdots$	0.18	$\cdots$	-0.15
QCDSR-I (1 GeV) [112]	0.79	0.36	-1.832	-2.1×10^{-2}
QCDSR-II (1 GeV) [112]	0.74	0.30	-1.64	-2.5×10^{-2}
Skyrme [31]	1	0.5	-3.584	$\cdots$
Skyrme [32]	1	0.5	-2.832	$\cdots$
χQSM [28]	1	0.5	-1.88	$\cdots$
Soliton model [113]	1	0.5	-4.024	$\cdots$
χQSM [29]	$\cdots$	$\cdots$	-3.88	$\cdots$
χQSM [114]	1	0.5	-2.60	$\cdots$
AdS/QCD model I [41]	0.917	0.415	$\cdots$	$\cdots$
AdS/QCD model II [41]	0.8742	0.392	$\cdots$	$\cdots$
LCSR-LO [33]	$\cdots$	$\cdots$	-2.104	$\cdots$
KM15 fit [115]	$\cdots$	$\cdots$	-1.744	$\cdots$
DR [39]	$\cdots$	$\cdots$	-1.36	$\cdots$
JLab data [5]	$\cdots$	$\cdots$	-1.688	$\cdots$
IP [21]	$\cdots$	$\cdots$	$\cdots$	1.4×10^{-2}

Addressing this by including gluonic contributions in the computation of the genuine $\bar{C}_q$ form factors is planned for future work. The evolved results for the GFFs obtained from the DGLAP evolution equation include only the contributions from perturbative partons. The evolution process does not account for nonperturbative gluonic contributions. In particular, our current analysis considers only the valence Fock state of the proton at the initial scale, so it does not include contributions from nonperturbative gluons. To study the nonperturbative gluonic contributions to the GFFs, we would need to incorporate dynamical gluons that enter the Fock space expansion of the proton state. Guidance on the importance of the gluonic contributions to the structure of the proton can be seen in their role in the protons $\bar{C}$ form factor which were estimated using the instanton vacuum in Ref. [21].

In Table II, we provide a detailed overview of the GFFs at $Q^2 = 0$. We compare them with predictions from various phenomenological models, lattice QCD, and the current experimental data for $D_q(0)$. For the form factors $A_q(0)$ and $J_q(0)$, our estimates are generally consistent, albeit slightly lower than the projections from Refs. [4,24,44–46,48,49,103] at a renormalization scale of $\mu^2 = 4$ GeV^2. It is noteworthy that the QCD sum

rule (QCDSR) (I and II) suggests a higher value for $A_q(0)$, likely due to its use of a reduced scale, $\mu^2 = 1$ GeV^2 [112].

In the χQSM and Skyrme models, only quarks and antiquarks contribute to the nucleon's angular momentum, accounting for the entirety of it. This results in the relationship $2J_q(0) = A_q(0) = 1$. As for the AdS/QCD models, the results are given at the model's inherent scale, with u and d quarks collectively accounting for approximately 90% of the nucleon's momentum.

Regarding the form factor $D_q(0)$, we observe the following trends. Our estimate aligns more closely with the lattice QCD results [45,46,103], although it is slightly on the higher side. Comparatively, the predictions from QCDSR-I [112] and QCDSR-II [112] are in the same ballpark as our estimate, but with slight variations. On the other hand, model-based predictions such as those from the Skyrme model [31,32], along with the χQSM predictions [28,29,113], deviate more significantly from our results. Interestingly, the χPT model [24] and IFF model [4] provide results that resonate closely with our findings. The KM15 fit [115] and the JLab data [5] offer values that hover around our prediction, yet show minor differences. Examining the $\bar{C}_q^{u+d}(0)$ values in Table II, our

TABLE III. The mechanical properties: pressure p_0, energy density $\mathcal{E}$, and mechanical radius squared $\langle r^2_{\text{mech}} \rangle$ of nucleon. The results presented herein represent the quark contribution to the nucleon.

Approaches/models	p_0 [GeV/fm^3]	$\mathcal{E}$ [GeV/fm^3]	$\langle r^2_{\text{mech}} \rangle$ [fm^2]
This work ($\sqrt{0.195}$ GeV $\rightarrow$ 2 GeV)	0.47 ± 0.10	2.38 ± 0.80	0.73 ± 0.01
QCDSR set-I (1 GeV) [112]	0.67	1.76	0.54
QCDSR set-II (1 GeV) [112]	0.62	1.74	0.52
Skyrme model [31]	0.47	2.28	$\cdots$
Modified Skyrme model [32]	0.26	1.45	$\cdots$
χQSM [28]	0.23	1.70	$\cdots$
χQSM [114]	0.35	1.89	0.55
Soliton model [113]	0.58	3.56	$\cdots$
LCSM-LO [33]	0.84	0.92	0.54

result has the lowest magnitude. The value of $\bar{C}(Q^2 = 0)$, when summed over all partons, should be zero according to the sum rule. Our Hamiltonian, as shown in Eq. (1), is based on the valence Fock sector of the proton system, which consists of three quarks and lacks any gluonic degrees of freedom. Therefore, $\bar{C}^u_q(0)$ is expected to have a sign opposite to $\bar{C}^d_q(0)$ so that their total $\bar{C}^{u+d}_q(0) = 0$. While we do not achieve an exact zero, obtaining a small value of $\bar{C}^{u+d}_q(0) = 0.0024$ is desirable. This reflects the understanding that a genuine calculation of the $\bar{C}_q$ term requires extending beyond the valence Fock sector to include contributions from gluonic degrees of freedom.

All GFF outcomes were fitted using a two-parameter dipole function. Comprehensive details of this function and the derived parameter values can be found in Appendix A.

A. Mechanical properties

The (D)-term can be directly related to the pressure p_0 in the center of the nucleon and the mechanical radius squared r^2_{mech} as [3]

$$p_0 = -\frac{1}{24\pi^2 M_n} \int_0^\infty \mathrm{d}Q^2 Q^3 D(Q^2),$$

$$\langle r^2_{\text{mech}} \rangle = 6D(0) \left[\int_0^\infty \mathrm{d}Q^2 D(Q^2) \right]^{-1}. \qquad (18)$$

The energy density $\mathcal{E}$ can be obtained as follows [3]:

$$\mathcal{E} = \frac{M_n}{4\pi^2} \int_0^\infty \mathrm{d}Q^2 Q \left(A(Q^2) + \bar{C}(Q^2) + \frac{Q^2}{4M_n^2}(D(Q^2) \right.$$
$$\left. - B(Q^2)) \right). \qquad (19)$$

Here, M_n denotes the mass of nucleon. In Table III, we list our findings alongside those from various models and approaches. For the pressure, p_0, our results are closest to those of the Skyrme model [31] and the soliton model [113]. Regarding the energy density, $\mathcal{E}$, our value

is less than that predicted by the soliton model [113] but higher than most other predictions, including those from QCDSR [112] and LCSM-LO [33]. The energy density, similar to the pressure, aligns well with the prediction from the Skyrme model [31]. Note that the combination $A_q(0) + \bar{C}_q(0)$ is interpreted as the average energy density of a nucleon at rest, expressed in mass per unit volume [4,116]. Therefore, the mass decomposition is closely linked to this combination, and an accurate analysis of the mass decomposition necessitates the inclusion of gluonic degrees of freedom. Finally, concerning the mechanical radius squared, $\langle r^2_{\text{mech}} \rangle$, our prediction surpasses the values reported in Refs. [33,112,114]. We emphasize that the effective Hamiltonian utilized in this investigation, as depicted in Eq. (1), pertains solely to the three quarks within the valence Fock sector of the proton. Consequently, our findings exclude the gluonic contribution and highlight solely the quark contribution within the valence Fock sector. The crucial gluon contribution will be computed in future research.

1. Pressure and shear forces

In our study, the D-term is derived from the transverse components of the EMT, which have connections to mechanical properties like the pressure and shear distributions [3,21,110,117]. A deeper understanding of these quantities can be achieved by undertaking a 2D Fourier transformation (FT) of the D-term with respect to the transverse momentum transfer thereby transitioning from momentum space to impact parameter space.

The FT $[\tilde{D}(b)]$ of the D-term can be expressed using the Bessel function of the zeroth order (J_0) as follows:

$$\tilde{D}(b) = \frac{1}{(2\pi)^2} \int d^2 \mathbf{q}^\perp e^{-i\mathbf{q}^\perp \cdot \mathbf{b}^\perp} D(q^2),$$

$$= \frac{1}{2\pi} \int_0^\infty dq^{\perp 2} J_0(\mathbf{q}^\perp \mathbf{b}^\perp) D(q^2), \qquad (20)$$

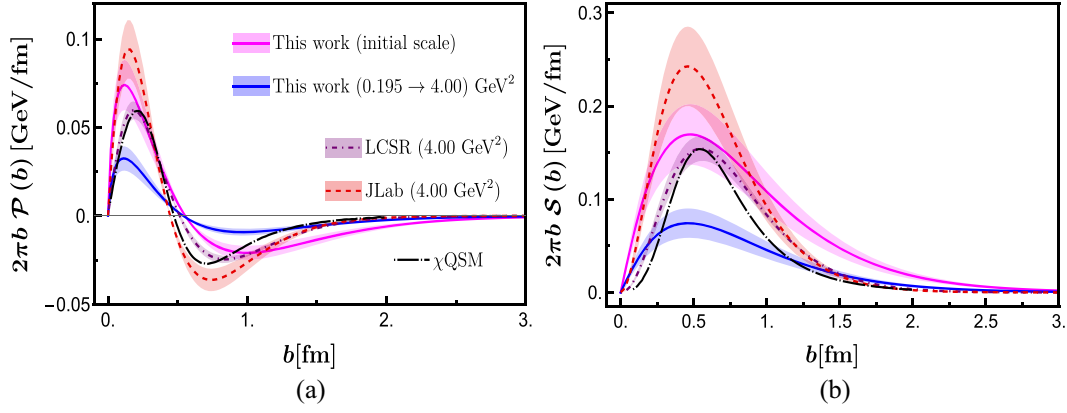where, $b = |\vec{b}_\perp|$ represents the impact parameter.

FIG. 3. Plots of (a) the pressure distribution $2\pi b\, \mathcal{P}(b)$, and (b) the shear force distribution $2\pi b\, \mathcal{S}(b)$ as a function of b. Our results are compared with results based on LCSR evaluated in Ref. [33] (purple dot-dashed lines) and using the fitting function of $D(Q^2)$ based on JLab experimental data [5] (red dashed lines). Additionally, we draw comparisons to the results from the χQSM for the nucleon with flavor SU(3) symmetry as presented in Ref. [114], indicated by the dot-dashed black line. The solid magenta lines with magenta bands and the solid blue lines with blue bands represent the results at the initial scale $\mu_0^2 = 0.195 \pm 0.020\ \mathrm{GeV}^2$ and the final evolved scale of $\mu^2 = 4.00\ \mathrm{GeV}^2$, respectively. The systematic uncertainties presented in the experimental extraction of the D-term [5] were added in quadrature.

The 2D pressure $p(b)$ and shear distributions $s(b)$ can thus be defined in the impact parameter space as follows [118,119]:

$$p(b) = \frac{1}{8P^+} \frac{1}{b} \frac{d}{db}\left[b \frac{d}{db} \tilde{D}_q(b) \right],$$

$$s(b) = -\frac{1}{4P^+} b \frac{d}{db}\left[\frac{1}{b} \frac{d}{db} \tilde{D}_q(b) \right], \qquad (21)$$

where P^+ denote the light cone total longitudinal momentum. The densities described in Eq. (21) are scaled by the Lorentz factor for practical purposes, as outlined in [119], resulting in the following expressions:

$$\mathcal{P}(b) = \frac{P^+}{2M} p(b), \qquad (22)$$

$$\mathcal{S}(b) = \frac{P^+}{2M} s(b). \qquad (23)$$

A spherical shell of radius b experiences normal and tangential forces, which are defined by the combined effects of pressure and shear [3],

$$F_n(b) = \left(\mathcal{P}(b) + \frac{1}{2}\mathcal{S}(b) \right), \qquad (24)$$

$$F_t(b) = \left(\mathcal{P}(b) - \frac{1}{2}\mathcal{S}(b) \right). \qquad (25)$$

In Fig. 3, we present the 2D pressure $[2\pi b\, \mathcal{P}(b)]$ and shear distributions $[2\pi b\, \mathcal{S}(b)]$ as functions of the impact parameter b. Our results are compared with analyses from

the LCSR [33], the χQSM for the nucleon with flavor SU (3) symmetry [114], and experimental data from JLab using fitting functions for $D(Q^2)$ [5]. The conservation of the EMT also informs the 2D stability condition of the nucleon, with the pressure and shear force distributions playing fundamental roles in this stability condition. The 2D equilibrium equation, derived from the conservation of the EMT current, is given by [118]

$$\mathcal{P}'(b) + \frac{1}{2}\mathcal{S}'(b) + \frac{1}{b}\mathcal{S}(b) = 0. \qquad (26)$$

Furthermore, the pressure and shear distributions must adhere to the von Laue condition and its lower-dimensional subsystem within the nucleon, expressed as follows [114]:

$$\int_0^\infty d^2b\, \mathcal{P}(b) = 0,$$

$$\int_0^\infty db \left[\mathcal{P}(b) - \frac{1}{2}\mathcal{S}(b) \right] = 0. \qquad (27)$$

We confirm the global stability condition, as shown in Eq. (27), through numerical integration. The results, summarized in Table IV, approximate zero within the limits

TABLE IV. Numerical values for the stability condition shown in Eq. (27) at the initial and the evolved final scale.

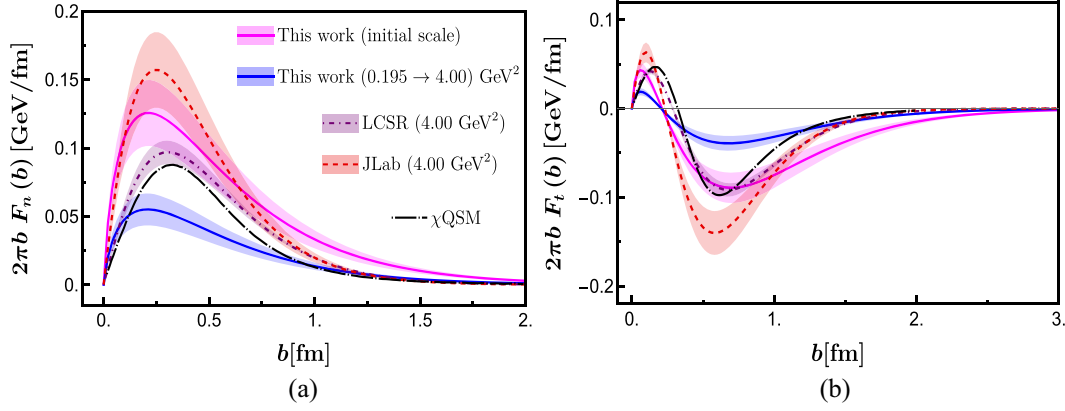| Stability condition	Initial scale $(\sqrt{0.195}\ \mathrm{GeV})$	Final scale $(2\ \mathrm{GeV})$
$\int_0^\infty d^2b\, \mathcal{P}(b)$	-2.39×10^{-15}	-4.38×10^{-15}
$\int_0^\infty db[\mathcal{P}(b) - \frac{1}{2}\mathcal{S}(b)]$	-7.03×10^{-10}	-3.80×10^{-10}

FIG. 4. Plots of (a) the normal forces F_n, and (b) the tangential forces F_t as a function of b. The legends are same as mentioned in Fig. 3.

of numerical precision, affirming the validity of our approach under the uncertainty of numerical calculations. The von Laue condition arises from the need to balance internal forces in a system [3,110], indicating that the distribution should have a point where it changes sign. Our data shows a positive region followed by a negative region, suggesting the presence of both outward-pushing and inward-pulling forces within the nucleon. In our results, the point where the pressure changes sign is approximately $b \approx 0.6$ fm for both scales. For the light cone sum rule [33], this point is at $b \approx 0.51$ fm, and for the JLab data [5], it is around $b \approx 0.45$ fm. For the χQSM, this point lies between the JLab and LCSR, but closer to the JLab crossing point. Even though the zero crossings in our model occur somewhat later than those in the comparative datasets, the overarching characteristics and mechanical implications of the pressure distribution align across different models and empirical findings [6,28,31–33,113].

This shear distribution is associated with attributes like surface tension and surface energy, which are typically positive in stable hydrostatic systems [3]. In line with previous studies, our results confirm that the shear distribution remains positive across all b values, thus satisfying the local stability condition $\mathcal{S}(b) > 0$. Furthermore, the behavior of our shear force distribution is consistent with outcomes from other methodologies [6,28,31–33,113]. It appears to be a coincidence that our initial scale results for both pressure and shear align more closely with the light cone sum rule [33], χQSM [114], and the JLab data [5] than the evolved results. Additionally, the peak position of our results at the final scale occurs at a lower value of b.

In Figs. 4(a) and 4(b), we present our results for the normal and tangential forces attributed to the valence quark combination, respectively. A salient observation is the consistently positive nature of $F_n(b)$. We thus find that the local stability condition pertaining to $F_n(b) = \mathcal{P}(b) + \frac{1}{2}\mathcal{S}(b) > 0$ is also satisfied. On the other hand, $F_t(b)$ showcases a dual character: a positive core, indicative of

repulsive forces, and a subsequent negative domain, signifying attractive forces, with the transition (zero-crossing) located around $b \approx 0.4$ fm. The peak of the repulsive force occurs close to $b \approx 0.3$ fm, while the maximum attractive force, which plays a pivotal role in binding, is more pronounced around $b \approx 0.6$ fm. It is worth noting that this binding force exhibits a greater magnitude than the repulsive counterpart. Thus, within the BLFQ framework, the key features of these forces exhibit good agreement with insights from the light cone sum rule [33], the distributions inferred from JLab's $D(Q^2)$ fitting function [5], and the predictions of the chiral quark-soliton model [114]. We further explore the normal and tangential force by plotting them as vector fields in the impact parameter space in Fig. 5. We observe that the normal force fields $2\pi b F_n(b)\hat{e}_r$ are directed outwards, while the tangential force fields are found to rotate inside the nucleon. The inner part of $2\pi b F_t(b)\hat{e}_\theta$ rotates anticlockwise, whereas the outer part rotates clockwise. These observed patterns in the vector plots facilitate the visualization of the crucial requirements for a stable nucleon.

2. The Galilean energy density and pressure distributions

Within the context of nucleonic internal structures, understanding energy density and pressure distributions offers invaluable insights. To this end, we have drawn upon the Galilean framework to study these distributions, as described in Ref. [4]. We represent the Galilean energy density $\mu(b)$, radial pressure $\sigma^r(b)$, tangential pressure $\sigma^t(b)$, isotropic pressure $\sigma(b)$, and pressure anisotropy $\Pi(b)$ through the equations below,

$$\mu(b) = M \left[\frac{A(b)}{2} + \bar{C}(b) + \frac{1}{4M^2}\frac{1}{b}\frac{d}{db} \right. \\ \left. \times \left(b\frac{d}{db}\left[\frac{B(b)}{2} - 4C(b) \right] \right) \right], \quad (28)$$
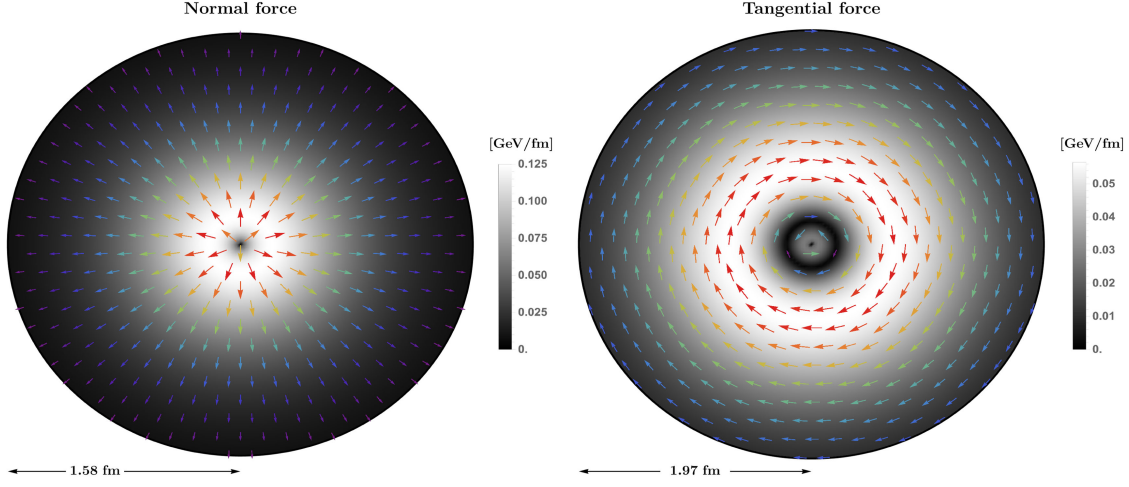
FIG. 5. Vector plot showcasing the normal and tangential forces at the initial scale in the transverse plane (b_x, b_y), where the impact parameter b is defined as $b = \sqrt{b_x^2 + b_y^2}$. The normal force is represented as $2\pi b F_n(b)\hat{e}_r$, and the tangential force as $2\pi b F_t(b)\hat{e}_\theta$. Here, $\hat{e}_r$ and $\hat{e}_\theta$ denote the polar unit vectors, related to the Cartesian unit vectors by $\hat{e}_r = \cos(\theta)\hat{i} + \sin(\theta)\hat{j}$ and $\hat{e}_\theta = -\sin(\theta)\hat{i} + \cos(\theta)\hat{j}$, where $\theta = \tan^{-1}(b_x/b_y)$.

$$\sigma^r(b) = M\left[-\bar{C}(b) + \frac{1}{M^2}\frac{1}{b}\frac{dC(b)}{db}\right], \qquad (29)$$

$$\sigma^t(b) = M\left[-\bar{C}(b) + \frac{1}{M^2}\frac{d^2C(b)}{d(b)^2}\right], \qquad (30)$$

$$\sigma(b) = M\left[-\bar{C}(b) + \frac{1}{2}\frac{1}{M^2}\frac{1}{b}\frac{d}{db}\left(b\frac{dC(b)}{db}\right)\right], \qquad (31)$$

$$\Pi(b) = M\left[-\frac{1}{M^2}b\frac{d}{db}\left(\frac{1}{b}\frac{dC(b)}{db}\right)\right]. \qquad (32)$$

In Fig. 6, we present our findings for $2\pi b \mu$ which encompasses all four GFFs as per Eq. (28). The energy density's peak at the initial scale is discerned around $b \approx 0.4$ fm. However, when evolved, this peak not only diminishes in magnitude but also repositions closer, at $b \approx 0.3$ fm.

Turning to Fig. 7, we elaborate on the results for the pressures defined in Eqs. (29)–(32). The radial pressure remains consistently positive, indicating a repulsive nature. The tangential pressure, on the other hand, displays a more varied behavior; its positive (repulsive) region is located at smaller impact parameters, while the negative (attractive) region spans towards the larger values of b. The isotropic pressure and the pressure anisotropy are essentially linear combinations of the radial and tangential pressures. Specifically, they are defined by the relations $\sigma = \frac{(\sigma_r + \sigma_t)}{2}$ and $\Pi = \sigma_r - \sigma_t$. We observe that the isotropic pressure largely mirrors the behavior of the radial pressure, though it turns slightly negative for larger b values, specifically beyond 1.0 fm. The pressure anisotropy remains positive everywhere, implying that the radial pressure consistently exceeds the tangential one.

Our projections for these energy and pressure distributions align well with a straightforward multipole model as proposed in Ref. [4]. An interesting coincidence is that our results at the scale $\mu^2 = 4.00$ GeV^2 align more closely with the multipole model than those at the initial scale of $\mu_0^2 = 0.195$ GeV^2.
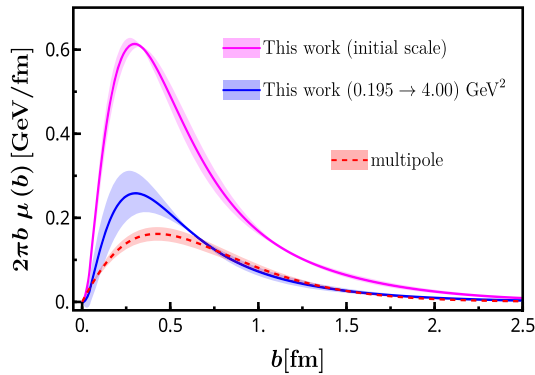

FIG. 6. Plot of the two-dimensional Galilean energy density $2\pi b \mu_q(b)$. The solid magenta line with magenta bands and the solid blue line with blue bands represent the results at the initial scale $\mu_0^2 = 0.195 \pm 0.020$ GeV^2 and $\mu^2 = 4$ GeV^2, respectively. Our results are compared with the results in a multipole model (red dashed line) [4] and the red band denotes a 10% uncertainty in the parameter $F_q(0)$ as defined in [4].
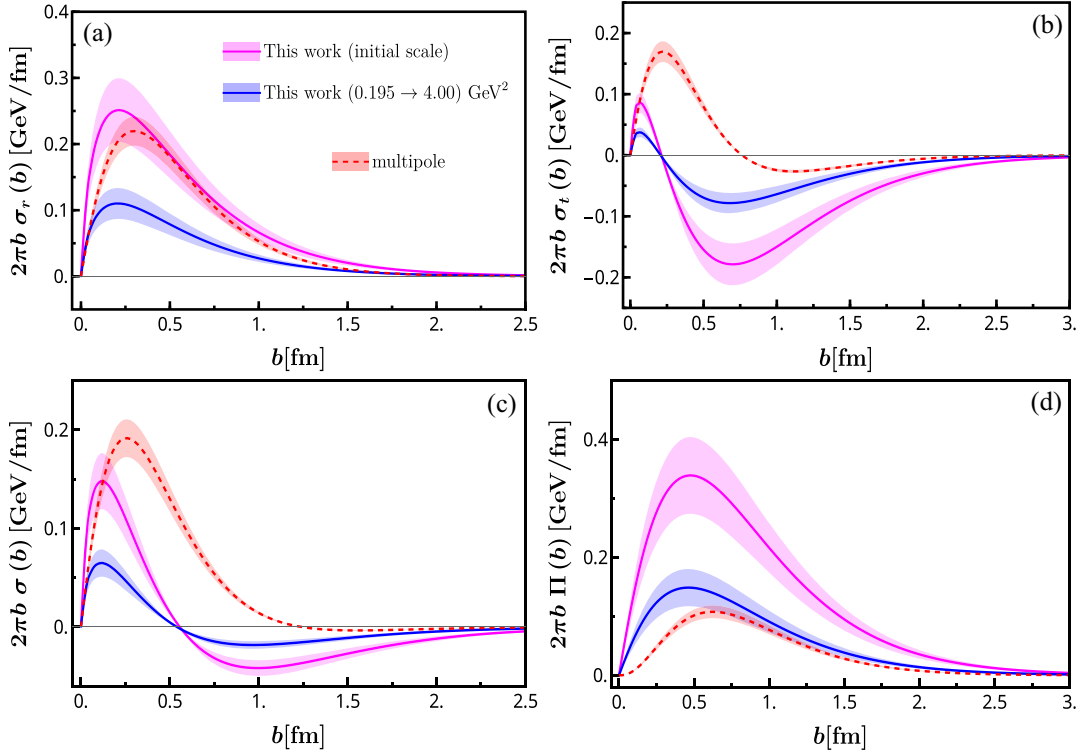
FIG. 7. Plots of the two-dimensional radial pressure (a) $2\pi b\,\sigma_r$, (b) tangential pressure $2\pi b\,\sigma_t$, (c) isotropic pressure $2\pi b\,\sigma$ and (d) the pressure anisotropy $2\pi b\,\Pi$. The legends are same as mentioned in Fig. 6.

V. CONCLUSION

In this study, we delved into the GFFs and the mechanical attributes of quarks in the proton using the BLFQ theoretical approach. Utilizing an effective light-front Hamiltonian, we integrated confinement across both transverse and longitudinal planes, coupled with a one-gluon exchange interaction tailored for valence quarks, making it apt for low-resolution applications. By treating the Hamiltonian as a relativistic three-quark problem within the BLFQ framework, we deduced the nucleon LFWFs as its eigenvectors. These LFWFs then served as the foundation to derive the quark GFFs.

We evaluated the four GFFs and studied their Q^2 dependence at both the initial scale of $\mu_0^2 = 0.195$ GeV^2 and final evolved scale of $\mu^2 = 4.00$ GeV^2. The $A(Q^2)$ and $B(Q^2)$ GFFs are comparable with lattice QCD results [103] although our result for the $A(Q^2)$ is slightly lower compared to lattice QCD result. We have observed that our result for $D(Q^2)$ is in qualitative accord with the experimental data extracted from DVCS process at JLab [5] and lattice QCD predictions [103]. We fitted our GFFs to a dipole function with two parameters as discussed in Appendix A. We have compared the values of the GFFs at $Q^2 = 0$ with the existing theoretical predictions and the data from JLab. Our estimates for $A_q(0)$ and $J_q(0)$ align reasonably with multiple references, though they tend to be

slightly lower at a renormalization scale of $\mu^2 = 4$ GeV^2. For the $D_q(0)$ form factor, our results are largely in sync with lattice QCD. Our $\bar{C}_q^{u+d}(0)$ value is found to be close to zero such that $\bar{C}_q^u(0) > 0$ and $\bar{C}_q^d(0) < 0$ since both have the same shapes, opposite signs and nearly the same magnitudes.

Using GFFs in the BLFQ framework, we assessed the proton's internal pressure, energy density, and mechanical radius, comparing with other theoretical models. The central proton pressure, p_0, aligns best with Skyrme [31] and soliton models [113]. Our energy density, $\mathcal{E}$, situates between LCSM-LO [33] and other predictions like QCDSR [112]. Despite varying theoretical predictions on p_0 and $\mathcal{E}$, our mechanical radius, $\langle r_{\text{mech}}^2 \rangle$, is notably larger than in Refs. [33,112].

In the BLFQ framework, we analyzed the internal pressure $p(b)$ and shear force $s(b)$ distributions within the proton. We observed a positive core and a negative tail for $p(b)$, while $s(b)$ remained consistently positive, aligning with both experimental data and other theoretical models. Additionally, the normal force $F_n(b)$ is uniformly repulsive, whereas the tangential force $F_t(b)$ shows repulsion at the center but attraction towards the periphery. These patterns generally concur with experimental and theoretical expectations. Moreover, our computations of the two-dimensional Galilean energy density, various pressure

metrics, and anisotropy in the BLFQ framework match well qualitatively with a multipole model, especially for evolved results at higher scales.

The results showcased validate the efficacy of our effective Hamiltonian method in the BLFQ framework, encouraging its use for other hadrons. Our future plans will focus on calculating the gluon GFFs within the proton system by expanding the Fock space to include an additional dynamical gluon.

ACKNOWLEDGMENTS

APPENDIX A: GFFS FITTED WITH A DIPOLE FUNCTION

We fit both the initial and final scale GFFs with the following function:

$$f(Q^2) = \frac{a_0}{(1 + a_1 Q^2)^2}. \tag{A1}$$

The fit parameters for the form factors $A(Q^2)$ and $B(Q^2)$ are listed in Table V. Parameters for $D(Q^2)$ and $\bar{C}(Q^2)$ are provided in Table VI. It should be emphasized that the fit for $\bar{C}(Q^2)$ is only reliable for $Q^2 > 0.2$, as its fitting function does not faithfully represent $\bar{C}(Q^2 \approx 0)$. The efficacy of the fit is evaluated through the χ^2 values presented for each GFF in Tables V and VI, calculated using Eq. (A2). In this equation, N denotes the number of data points, $N_p = 2$ represents the count of parameters, O_i are the calculated GFF values according to the BLFQ framework, and C_i are the values obtained from the fitting procedure. The summation in Eq. (A2) encompasses all data points for which $0 \le Q^2 \le 2$ for the GFFs, except for $\bar{C}(Q^2)$, where the condition is $0.2 \le Q^2 \le 2$,

$$\chi^2 = \frac{1}{(N - N_p - 1)} \sum_i \frac{(O_i - C_i)^2}{|C_i|}. \tag{A2}$$

TABLE V. Fit parameters for $A(Q^2)$ and $B(Q^2)$ for u and d quark flavor. The unprimed parameters (a_i) are for the initial scale of $\mu_0^2 = 0.195$ GeV^2 and the primed parameters (a_i') for the final scale of $\mu^2 = 2$ GeV^2. The upper and lower bounds denote the error bands around the main value. The χ^2 values indicate the goodness of fit calculated using Eq. (A2). For the calculation of each χ^2 value, we made use of 29 distinct points across the interval $0 \le Q^2 \le 2$.

GFF	Bound	a_0	a_1	χ^2	a_0'	a_1'	χ^2
$A^u(Q^2)$	Central	0.6731	0.7762	0.00010378	0.2837	0.7764	0.00005875
$A^u(Q^2)$	Upper	0.6787	0.6116	0.00015951	0.3034	0.6924	0.00011753
$A^u(Q^2)$	Lower	0.6703	0.9167	0.00012235	0.2643	0.8863	6.5513×10^{-6}
$A^d(Q^2)$	Central	0.3188	0.9112	0.00001585	0.1338	0.9134	0.00001145
$A^d(Q^2)$	Upper	0.3099	0.7733	0.00003394	0.1435	0.8714	0.00003479
$A^d(Q^2)$	Lower	0.3220	1.0310	0.00002023	0.1241	0.9640	3.9597×10^{-7}
$B^u(Q^2)$	Central	0.3289	1.1102	2.1633×10^{-6}	0.1398	1.1169	3.0792×10^{-7}
$B^u(Q^2)$	Upper	0.3195	0.9266	9.8522×10^{-6}	0.1494	1.0434	9.6802×10^{-6}
$B^u(Q^2)$	Lower	0.3285	1.2743	5.0886×10^{-6}	0.1303	1.2067	0.00002466
$B^d(Q^2)$	Central	-0.3279	1.0171	6.2102×10^{-6}	-0.1393	1.0227	3.8685×10^{-6}
$B^d(Q^2)$	Upper	-0.3185	0.8624	0.00003352	-0.1296	1.0929	3.5263×10^{-6}
$B^d(Q^2)$	Lower	-0.3274	1.1574	3.7700×10^{-6}	-0.1489	0.9649	0.00002398

TABLE VI. Fit parameters for $D(Q^2)$ and $\bar{C}(Q^2)$ for both u and d quark flavor. The unprimed parameters (a_i) are for the initial scale of $\mu_0^2 = 0.195$ GeV^2 and the primed parameter (a_i') are for the final scale of $\mu^2 = 2$ GeV^2. The upper and lower bounds denote the error bands around the main value. The χ^2 values indicate the goodness of fit calculated using Eq. (A2). To determine the χ^2 values for the GFF $D(Q^2)$, we utilized a set of 29 discrete data points spanning the range $0 \leq Q^2 \leq 2$. For the GFF $\bar{C}(Q^2)$, we calculated using 20 discrete data points within the interval $0.2 \leq Q^2 \leq 2$.

GFF	Bound	a_0	a_1	χ^2	a_0'	a_1'	χ^2
$D^u(Q^2)$	Central	-2.8330	3.1549	0.00008020	-1.1460	2.9875	0.00011587
$D^u(Q^2)$	Upper	-3.4741	3.1525	0.00106679	-0.9571	3.0757	0.00054817
$D^u(Q^2)$	Lower	-2.5569	3.2365	0.00034558	-1.3347	2.9243	0.00010448
$D^d(Q^2)$	Central	-1.9610	3.5540	0.00011851	-0.7822	3.3392	0.00017370
$D^d(Q^2)$	Upper	-2.6775	3.687	0.00020343	-0.5869	3.2820	0.00041175
$D^d(Q^2)$	Lower	-1.6696	3.5211	0.00040762	-0.9776	3.3753	0.00010373
$\bar{C}^u(Q^2 \geq 0.2)$	Central	0.4924	0.7259	0.00016296	0.2126	0.7298	0.00023901
$\bar{C}^u(Q^2 \geq 0.2)$	Upper	0.5856	0.6157	0.00006947	0.2393	0.6349	0.00023820
$\bar{C}^u(Q^2 \geq 0.2)$	Lower	0.4732	0.8198	0.00013749	0.1892	0.8969	0.00029638
$\bar{C}^d(Q^2 \geq 0.2)$	Central	-0.4257	0.6935	0.00011733	-0.1839	0.7011	0.00015369
$\bar{C}^d(Q^2 \geq 0.2)$	Upper	-0.5426	0.6545	0.00003208	-0.1531	0.7846	0.00017627
$\bar{C}^d(Q^2 \geq 0.2)$	Lower	-0.3988	0.7485	0.00010404	-0.2154	0.6509	0.00014935

APPENDIX B: HO INTEGRALS USED FOR CALCULATING $C_q(Q^2)$ AND $\bar{C}_q(Q^2)$

The recurrence relation for the HO wave function is as follows [71]:

$$k\phi_{n,m}(\vec{k}_\perp) = b \begin{cases} \sqrt{n+|m|+1}\,\phi_{n,m+1}(\vec{k}_\perp) - H(n-1)\sqrt{n}\,\phi_{n-1,m+1}(\vec{k}_\perp) & ; m \geq 0 \\ \sqrt{n+|m|}\,\phi_{n,m+1}(\vec{k}_\perp) - \sqrt{n+1}\,\phi_{n+1,m+1}(\vec{k}_\perp) & ; m < 0, \end{cases} \tag{B1}$$

$$k^*\phi_{n,m}(\vec{k}_\perp) = b \begin{cases} \sqrt{n+|m|+1}\,\phi_{n,m-1}(\vec{k}_\perp) - H(n-1)\sqrt{n}\,\phi_{n-1,m-1}(\vec{k}_\perp) & ; m < 0 \\ \sqrt{n+|m|}\,\phi_{n,m-1}(\vec{k}_\perp) - \sqrt{n+1}\,\phi_{n+1,m-1}(\vec{k}_\perp) & ; m \geq 0, \end{cases} \tag{B2}$$

where k is the complex representation of $\vec{k}_\perp$ such that $k = \vec{k}_\perp^{(1)} + i\vec{k}_\perp^{(2)}$ and the HO wave function is as defined in Eq. (3). $H(n)$ is the unit step function. The following integrals were utilized when evaluating the GFFs $C_q(Q^2)$ and $\bar{C}_q(Q^2)$ and they are derived form the recurrence relation shown above:

$$\mathcal{I}_1 = \int_{-\infty}^{\infty} d^2k_\perp k_\perp^{(1)} \times \phi_{n,m}^*(\vec{k}_\perp, b_1)\phi_{n',m'}(\vec{k'}_\perp, b_2)$$
$$= \frac{1}{2}\left(\mathcal{OI}_1(x, b_1, n, m, b_2, n', m', q^{(1)}, q^{(2)}) + \mathcal{OI}_1^*(x, b_1, n, m, b_2, n', m', q^{(1)}, q^{(2)})\right), \tag{B3}$$

$$\mathcal{I}_2 = \int_{-\infty}^{\infty} k_\perp^{(2)} \times \phi_{n,m}^*(\vec{k}_\perp, b_1)\phi_{n',m'}(\vec{k'}_\perp, b_2)$$
$$= -\frac{i}{2}\left(\mathcal{OI}_1(x, b_1, n, m, b_2, n', m', q^{(1)}, q^{(2)}) - \mathcal{OI}_1^*(x, b_1, n, m, b_2, n', m', q^{(1)}, q^{(2)})\right), \tag{B4}$$

$$\mathcal{I}_{12} = \int_{-\infty}^{\infty} k_\perp^{(1)} k_\perp^{(2)} \times \phi_{n,m}^*(\vec{k}_\perp, b_1)\phi_{n',m'}(\vec{k'}_\perp, b_2)$$
$$= -\frac{i}{4}\left(\mathcal{OI}_2(x, b_1, n, m, b_2, n', m', q^{(1)}, q^{(2)}) - \mathcal{OI}_2^*(x, b_1, n, m, b_2, n', m', q^{(1)}, q^{(2)})\right), \tag{B5}$$

$$\mathcal{I}_{11} = \int_{-\infty}^{\infty} k_{\perp}^{(1)} k_{\perp}^{(1)} \times \phi_{n,m}^*(\vec{k}_{\perp}, b_1) \phi_{n',m'}(\vec{k'}_{\perp}, b_2)$$

$$= \frac{1}{4} \Big(\mathcal{OI}_2(x, b_1, n, m, b_2, n', m', q^{(1)}, q^{(2)}) + \mathcal{OI}_2^*(x, b_1, n, m, b_2, n', m', q^{(1)}, q^{(2)})$$

$$+ 2\mathcal{OI}_{12}(x, b_1, n, m, b_2, n', m', q^{(1)}, q^{(2)}) \Big), \tag{B6}$$

$$\mathcal{I}_{22} = \int_{-\infty}^{\infty} k_{\perp}^{(2)} k_{\perp}^{(2)} \times \phi_{n,m}^*(\vec{k}_{\perp}, b_1) \phi_{n',m'}(\vec{k'}_{\perp}, b_2)$$

$$= -\frac{1}{4} \Big(\mathcal{OI}_2(x, b_1, n, m, b_2, n', m', q^{(1)}, q^{(2)}) + \mathcal{OI}_2^*(x, b_1, n, m, b_2, n', m', q^{(1)}, q^{(2)})$$

$$- 2\mathcal{OI}_{12}(x, b_1, n, m, b_2, n', m', q^{(1)}, q^{(2)}) \Big), \tag{B7}$$

where $\vec{k'}_{\perp} = \vec{k}_{\perp} + (1-x)q_{\perp}$ and $k_{\perp}^{(j)}$ with $j = (1,2)$ are the transverse components of $\vec{k}_{\perp}$ such that $(k_{\perp}^{(1)})^2 + (k_{\perp}^{(2)})^2 = (k_{\perp})^2$. We take $b_1 = b_2 = b$. The functions $\mathcal{OI}$ are defined as follows:

$$\mathcal{OI}_1(x, b_1, n, m, b_2, n', m', q^{(1)}, q^{(2)})$$

$$= b\sqrt{x} \times \begin{cases} \sqrt{n' + |m'| + 1} \times \mathcal{OL}_{q^{(1)},q^{(2)}}^{b_1,b_2}(n, m, n', m' + 1) - H(n' - 1) \times \sqrt{n'} \times \mathcal{OL}_{q^{(1)},q^{(2)}}^{b_1,b_2}(n, m, n' - 1, m' + 1) & \text{if } m' \geq 0 \\ \sqrt{n' + |m'|} \times \mathcal{OL}_{q^{(1)},q^{(2)}}^{b_1,b_2}(n, m, n', m' + 1) - \sqrt{n' + 1} \times \mathcal{OL}_{q^{(1)},q^{(2)}}^{b_1,b_2}(n, m, n' + 1, m' + 1) & \text{otherwise} \end{cases}$$

$$\mathcal{OI}_1^*(x, b_1, n, m, b_2, n', m', q^{(1)}, q^{(2)})$$

$$= b\sqrt{x} \times \begin{cases} \sqrt{n' + |m'| + 1} \times \mathcal{OL}_{q^{(1)},q^{(2)}}^{b_1,b_2}(n, m, n', m' - 1) - H(n' - 1) \times \sqrt{n'} \times \mathcal{OL}_{q^{(1)},q^{(2)}}^{b_1,b_2}(n, m, n' - 1, m' - 1) & \text{if } m' \leq 0 \\ \sqrt{n' + |m'|} \times \mathcal{OL}_{q^{(1)},q^{(2)}}^{b_1,b_2}(n, m, n', m' - 1) - \sqrt{n' + 1} \times \mathcal{OL}_{q^{(1)},q^{(2)}}^{b_1,b_2}(n, m, n' + 1, m' - 1), & \text{otherwise} \end{cases}$$

$$\mathcal{OI}_2(x, b_1, n, m, b_2, n', m', q^{(1)}, q^{(2)}) = b^2 x f(n, m, n', m'), \tag{B8}$$

$$f(n, m, n', m') = \sqrt{n' + |m'| + 1} \Big(\sqrt{n' + |m' + 1| + 1} \mathcal{OL}_{q^{(1)},q^{(2)}}^{b_1,b_2}(n, m, n', m' + 2) \qquad \text{if } m' \geq 0$$

$$- H(n' - 1)\sqrt{n'} \mathcal{OL}_{q^{(1)},q^{(2)}}^{b_1,b_2}(n, m, n' - 1, m' + 2) \Big)$$

$$- H(n' - 1)\sqrt{n'} \Big(\sqrt{n' - 1 + |m' + 1| + 1} \mathcal{OL}_{q^{(1)},q^{(2)}}^{b_1,b_2}(n, m, n' - 1, m' + 2)$$

$$- H(n' - 2)\sqrt{n' - 1} \mathcal{OL}_{q^{(1)},q^{(2)}}^{b_1,b_2}(n, m, n' - 2, m' + 2) \Big), \tag{B9}$$

$$f(n, m, n', m') = \sqrt{n' + |m'|} \Big(\sqrt{n' + |m' + 1| + 1} \mathcal{OL}_{q^{(1)},q^{(2)}}^{b_1,b_2}(n, m, n', m' + 2) \qquad \text{if } m' = -1$$

$$- H(n' - 1)\sqrt{n'} \mathcal{OL}_{q^{(1)},q^{(2)}}^{b_1,b_2}(n, m, n' - 1, m' + 2) \Big)$$

$$- \sqrt{n' + 1} \Big(\sqrt{n' + 1 + |m' + 1| + 1} \mathcal{OL}_{q^{(1)},q^{(2)}}^{b_1,b_2}(n, m, n' + 1, m' + 2)$$

$$- H(n')\sqrt{n' + 1} \mathcal{OL}_{q^{(1)},q^{(2)}}^{b_1,b_2}(n, m, n', m' + 2) \Big), \tag{B10}$$

$$f(n, m, n', m') = \sqrt{n' + |m'|}\left(\sqrt{n' + |m' + 1|}\mathcal{OL}_{q^{(1)},q^{(2)}}^{b_1,b_2}(n, m, n', m' + 2)\right. \qquad \text{otherwise}$$

$$\left. -\sqrt{n' + 1}\mathcal{OL}_{q^{(1)},q^{(2)}}^{b_1,b_2}(n, m, n' + 1, m' + 2)\right)$$

$$-\sqrt{n' + 1}\left(\sqrt{n' + 1 + |m' + 1|}\mathcal{OL}_{q^{(1)},q^{(2)}}^{b_1,b_2}(n, m, n' + 1, m' + 2)\right.$$

$$\left. -\sqrt{n' + 2}\mathcal{OL}_{q^{(1)},q^{(2)}}^{b_1,b_2}(n, m, n' + 2, m' + 2)\right), \tag{B11}$$

$$\mathcal{OI}_2^*(x, b_1, n, m, b_2, n', m', q^{(1)}, q^{(2)}) = b^2 x f^*(n, m, n', m'), \tag{B12}$$

$$f^*(n, m, n', m') = \sqrt{n' + |m'| + 1}\left(\sqrt{n' + |m' - 1| + 1}\mathcal{OL}_{q^{(1)},q^{(2)}}^{b_1,b_2}(n, m, n', m' - 2)\right. \quad \text{if } m' \leq 0$$

$$\left. -H(n' - 1)\sqrt{n'}\mathcal{OL}_{q^{(1)},q^{(2)}}^{b_1,b_2}(n, m, n' - 1, m' - 2)\right)$$

$$-H(n' - 1)\sqrt{n'}\left(\sqrt{n' + |m' - 1|}\mathcal{OL}_{q^{(1)},q^{(2)}}^{b_1,b_2}(n, m, n' - 1, m' - 2)\right.$$

$$\left. -H(n' - 2)\sqrt{n' - 1}\mathcal{OL}_{q^{(1)},q^{(2)}}^{b_1,b_2}(n, m, n' - 2, m' - 2)\right), \tag{B13}$$

$$f^*(n, m, n', m') = \sqrt{n' + |m'|}\left(\sqrt{n' + |m' - 1| + 1}\mathcal{OL}_{q^{(1)},q^{(2)}}^{b_1,b_2}(n, m, n', m' - 2)\right. \qquad \text{if } m' = 1$$

$$\left. -H(n' - 1)\sqrt{n'}\mathcal{OL}_{q^{(1)},q^{(2)}}^{b_1,b_2}(n, m, n' - 1, m' - 2)\right)$$

$$-\sqrt{n' + 1}\left(\sqrt{n' + 1 + |m' - 1| + 1}\mathcal{OL}_{q^{(1)},q^{(2)}}^{b_1,b_2}(n, m, n' + 1, m' - 2)\right.$$

$$\left. -H(n')\sqrt{n' + 1}\mathcal{OL}_{q^{(1)},q^{(2)}}^{b_1,b_2}(n, m, n', m' - 2)\right), \tag{B14}$$

$$f^*(n, m, n', m') = \sqrt{n' + |m'|}\left(\sqrt{n' + |m' - 1|}\mathcal{OL}_{q^{(1)},q^{(2)}}^{b_1,b_2}(n, m, n', m' - 2)\right. \qquad \text{otherwise}$$

$$\left. -\sqrt{n' + 1}\mathcal{OL}_{q^{(1)},q^{(2)}}^{b_1,b_2}(n, m, n' + 1, m' - 2)\right)$$

$$-\sqrt{n' + 1}\left(\sqrt{n' + 1 + |m' - 1|}\mathcal{OL}_{q^{(1)},q^{(2)}}^{b_1,b_2}(n, m, n' + 1, m' - 2)\right.$$

$$\left. -\sqrt{n' + 2}\mathcal{OL}_{q^{(1)},q^{(2)}}^{b_1,b_2}(n, m, n' + 2, m' - 2)\right), \tag{B15}$$

$$\mathcal{OI}_{12}(x, b_1, n, m, b_2, n', m', q^{(1)}, q^{(2)}) = b^2 x g(n, m, n', m'), \tag{B16}$$

$$
\begin{aligned}
g(n, m, n', m') = \sqrt{n' + |m'| + 1} &\bigg(\sqrt{n' + |m' + 1|} \mathcal{OL}^{b_1, b_2}_{q^{(1)}, q^{(2)}}(n, m, n', m') \qquad \text{if } m' \geq 0 \\
&- \sqrt{n' + 1} \mathcal{OL}^{b_1, b_2}_{q^{(1)}, q^{(2)}}(n, m, n' + 1, m') \bigg) \\
&- H(n' - 1) \sqrt{n'} \bigg(\sqrt{n' - 1 + |m' + 1|} \mathcal{OL}^{b_1, b_2}_{q^{(1)}, q^{(2)}}(n, m, n' - 1, m') \\
&- \sqrt{n'} \mathcal{OL}^{b_1, b_2}_{q^{(1)}, q^{(2)}}(n, m, n', m') \bigg),
\end{aligned}
\tag{B17}
$$

$$
\begin{aligned}
g(n, m, n', m') = \sqrt{n' + |m'|} &\bigg(\sqrt{n' + |m' + 1| + 1} \mathcal{OL}^{b_1, b_2}_{q^{(1)}, q^{(2)}}(n, m, n', m') \qquad \text{otherwise} \\
&- H(n' - 1) \sqrt{n'} \mathcal{OL}^{b_1, b_2}_{q^{(1)}, q^{(2)}}(n, m, n' - 1, m') \bigg) \\
&- \sqrt{n' + 1} \bigg(\sqrt{n' + 1 + |m' + 1| + 1} \mathcal{OL}^{b_1, b_2}_{q^{(1)}, q^{(2)}}(n, m, n' + 1, m') \\
&- H(n') \sqrt{n' + 1} \mathcal{OL}^{b_1, b_2}_{q^{(1)}, q^{(2)}}(n, m, n', m') \bigg).
\end{aligned}
\tag{B18}
$$

The function $\mathcal{OL}^{b_1, b_2}_{q^{(1)}, q^{(2)}}$ represents the overlap of the HO wave function and its approximate analytic expression is shown in the following subsection.

1. The HO overlap

$$
H(n): \text{ unit step function,}
\tag{B19}
$$

$$
\theta = \tan^{-1}\left(\frac{b_2}{b_1}\right),
\tag{B20}
$$

$$
l_i = q^{(i)} \times \sin(2\theta) \times \frac{\sqrt{b_1^2 + b_2^2}}{2} \quad (i = 1, 2),
\tag{B21}
$$

$$
l = \sqrt{l_1^2 + l_2^2},
\tag{B22}
$$

$$
\mathcal{C}(b_1, b_2, \tilde{q}) = \begin{cases} 1 & \text{if } b_1 = b_2 \text{ and } \tilde{q} = 0 \\ \cos^{\tilde{q}}(2\theta) & \text{otherwise.} \end{cases}
\tag{B23}
$$

We represent by $\mathcal{OL}^{b_1, b_2}_{q^{(1)}, q^{(2)}}(n_1, m_1, n_2, m_2)$ the integral of the overlap between the harmonic oscillator wave function such that

$$
\mathcal{OL}^{b_1, b_2}_{q^{(1)}, q^{(2)}}(n_1, m_1, n_2, m_2) = \int_{-\infty}^{\infty} d^2 k_\perp \phi^*_{n_1, m_1}(\vec{k}_\perp, b_1) \phi_{n_2, m_2}(\vec{k}'_\perp, b_2),
\tag{B24}
$$

where $\vec{k}'_\perp = \vec{k}_\perp + (1 - x)q_\perp$.

The approximate analytic expression for the above overlap can be represented in the following form:

$$
\begin{aligned}
\mathcal{OL}^{b_1, b_2}_{q^{(1)}, q^{(2)}}(n_1, m_1, n_2, m_2) = H(n_1)H(n_2) &\times \left(\frac{b_1 b_2}{b_1^2 + b_2^2}\right) \times \sqrt{2n_1!(n_1 + |m_1|)!2n_2!(n_2 + |m_2|)!} \times (-1)^{n_1 + n_2} \\
&\times \mathcal{OL}'\left(\frac{1}{b_1}, n_1, m_1, \frac{1}{b_2}, n_2, m_2, q^{(1)}, q^{(2)}\right).
\end{aligned}
\tag{B25}
$$

For the case $l \neq 0$ we have

$$\mathcal{OL}'(b_1, n_1, m_1, b_2, n_2, m_2, q^{(1)}, q^{(2)}) = \exp\left(-\frac{l^2}{2}\right) \sum_{r=r_{\min}}^{r_{\max}} \left(\sum_{v=v_{\min}}^{v_{\max}} \left(\sum_{w=w_{\min}}^{w_{\max}} \left(\sum_{z=z_{\min}}^{z_{\max}} \mathcal{EV}_0(r, v, w, z)\right)\right)\right), \quad \text{(B26)}$$

$$\mathcal{EV}_0(r, v, w, z) = (-1)^{\tilde{q}-u+t} \cdot l^{s+t} \cdot \frac{1}{p!} \cdot \begin{pmatrix} \tilde{q}+r+s+t \\ \tilde{q}, r, s, t \end{pmatrix} \cdot \begin{pmatrix} \tilde{q} \\ u \end{pmatrix} \cdot \begin{pmatrix} r \\ v \end{pmatrix} \cdot \begin{pmatrix} s \\ w \end{pmatrix} \cdot \begin{pmatrix} t \\ z \end{pmatrix}$$
$$\cdot \mathcal{C}(b_1, b_2, \tilde{q}) \cdot \sin^r(2\theta) \cdot \sin^s(\theta) \cdot \cos^t(\theta) \cdot e^{-i \cdot (s-2w+t-2z) \cdot \tan^{-1}(l_2/l_1)}, \quad \text{(B27)}$$

$$r_{\min} = 0, \qquad\qquad r_{\max} = n_1 + n_2 + \frac{|m_1| - m_1}{2} + \frac{|m_2| + m_2}{2},$$

$$v_{\min} = \max\left(-n_2 - \frac{|m_2| + m_2}{2} + r, 0\right), \qquad v_{\max} = \min\left(n_1 + \frac{|m_1| - m_1}{2}, r\right),$$

$$w_{\min} = \max(0, r - m_1 - 2v), \qquad w_{\max} = \min\left(r_{\max} - r, n_1 + \frac{|m_1| - m_1}{2} - v\right),$$

$$z_{\min} = \begin{cases} \max(m_2 + 2v - r, 0, r_{\max} - r - w) & \text{if } b_1 = b_2 \\ \max(m_2 + 2v - r, 0) & \text{otherwise} \end{cases}, \qquad z_{\max} = \min\left(r_{\max} - r - w, n_2 + \frac{|m_2| + m_2}{2} - r + v\right),$$

$$s = m_1 + 2v + 2w - r, \qquad t = -m_2 - 2v + 2z + r,$$

$$\tilde{q} = n_1 + n_2 + \frac{|m_1| - m_1}{2} + \frac{|m_2| + m_2}{2} - r - w - z, \qquad u = n_1 + \frac{|m_1| - m_1}{2} - v - w,$$

$$p = \tilde{q} + r + s + t. \qquad\qquad\qquad\qquad\qquad\qquad\qquad\qquad\qquad \text{(B28)}$$

For the case $l = 0$ we have

$$\mathcal{OL}'(b_1, n_1, m_1, b_2, n_2, m_2, q^{(1)}, q^{(2)}) = \sum_{v=0}^{v_{\max}} (-1)^{\tilde{q}-u} \times \frac{1}{p!} \times \mathcal{C}(b_1, b_2, \tilde{q}) \times \sin(2\theta)^r \begin{pmatrix} p \\ \tilde{q} \end{pmatrix} \times \begin{pmatrix} r \\ v \end{pmatrix} \times \begin{pmatrix} \tilde{q} \\ u \end{pmatrix}, \quad \text{(B29)}$$

where

$$p = \tilde{q} + r,$$
$$\tilde{q} = n_1 + n_2 - 2v,$$
$$r = |m_1| + 2v,$$
$$u = n_1 - v,$$
$$v_{\max} = \min\left(\frac{n_1 + n_2}{2}, n_1\right).$$

---

[1] G. A. Miller, Charge density of the neutron, Phys. Rev. Lett. **99**, 112001 (2007).

[2] C. E. Carlson and M. Vanderhaeghen, Empirical transverse charge densities in the nucleon and the nucleon-to-Δ transition, Phys. Rev. Lett. **100**, 032004 (2008).

[3] M. V. Polyakov and P. Schweitzer, Forces inside hadrons: Pressure, surface tension, mechanical radius, and all that, Int. J. Mod. Phys. A **33**, 1830025 (2018).

[4] C. Lorcé, H. Moutarde, and A. P. Trawiński, Revisiting the mechanical properties of the nucleon, Eur. Phys. J. C **79**, 89 (2019).

[5] V. D. Burkert, L. Elouadrhiri, and F. X. Girod, The pressure distribution inside the proton, Nature (London) **557,** 396 (2018).

[6] P. E. Shanahan and W. Detmold, Pressure distribution and shear forces inside the proton, Phys. Rev. Lett. **122,** 072003 (2019).

[7] S. Stepanyan *et al.*, Observation of exclusive deeply virtual Compton scattering in polarized electron beam asymmetry measurements, Phys. Rev. Lett. **87,** 182002 (2001).

[8] F. X. Girod *et al.*, Measurement of deeply virtual Compton scattering beam-spin asymmetries, Phys. Rev. Lett. **100,** 162002 (2008).

[9] S. Diehl *et al.*, Extraction of beam-spin asymmetries from the hard exclusive π^+ channel off protons in a wide range of kinematics, Phys. Rev. Lett. **125,** 182001 (2020).

[10] N. d'Hose, E. Burtin, P. A. M. Guichon, and J. Marroncle, Feasibility study of deeply virtual Compton scattering using COMPASS at CERN, Eur. Phys. J. A **19,** 47 (2004).

[11] C. Adloff *et al.* (The H1 Collaboration), Elastic electro-production of rho mesons at HERA, Eur. Phys. J. C **13,** 371 (2000).

[12] C. Adloff *et al.*, Measurement of deeply virtual Compton scattering at HERA, Phys. Lett. B **517,** 47 (2001).

[13] S. Chekanov *et al.*, Measurement of deeply virtual Compton scattering at HERA, Phys. Lett. B **573,** 46 (2003).

[14] A. Airapetian *et al.*, Measurement of the beam spin azimuthal asymmetry associated with deeply virtual Compton scattering, Phys. Rev. Lett. **87,** 182001 (2001).

[15] L. Favart, M. Guidal, T. Horn, and P. Kroll, Deeply virtual meson production on the nucleon, Eur. Phys. J. A **52,** 158 (2016).

[16] N. d'Hose, S. Niccolai, and A. Rostomyan, Experimental overview of deeply virtual Compton scattering, Eur. Phys. J. A **52,** 151 (2016).

[17] K. Kumericki, S. Liuti, and H. Moutarde, GPD phenom-enology and DVCS fitting: Entering the high-precision era, Eur. Phys. J. A **52,** 157 (2016).

[18] R. Abdul Khalek *et al.*, Science requirements and detector concepts for the electron-ion collider: EIC yellow report, Nucl. Phys. **A1026,** 122447 (2022).

[19] D. P. Anderle *et al.*, Electron-ion collider in China, Front. Phys. **16,** 64701 (2021).

[20] X.-D. Ji, Gauge-Invariant decomposition of nucleon spin, Phys. Rev. Lett. **78,** 610 (1997).

[21] M. V. Polyakov and H.-D. Son, Nucleon gravitational form factors from instantons: Forces between quark and gluon subsystems, J. High Energy Phys. 09 (2018) 156.

[22] J.-W. Chen and X.-d. Ji, Leading chiral contributions to the spin structure of the proton, Phys. Rev. Lett. **88,** 052003 (2002).

[23] A. V. Belitsky and X. Ji, Chiral structure of nucleon gravitational form-factors, Phys. Lett. B **538,** 289 (2002).

[24] M. Dorati, T. A. Gail, and T. R. Hemmert, Chiral pertur-bation theory and the first moments of the generalized parton distributions in a nucleon, Nucl. Phys. **A798,** 96 (2008).

[25] P. Schweitzer, S. Boffi, and M. Radici, Polynomiality of unpolarized off forward distribution functions and the D

[26] M. Wakamatsu and Y. Nakakoji, Generalized form factors, generalized parton distributions and the spin contents of the nucleon, Phys. Rev. D **74,** 054006 (2006).

[27] K. Goeke, J. Grabis, J. Ossmann, P. Schweitzer, A. Silva, and D. Urbano, The pion mass dependence of the nucleon form-factors of the energy momentum tensor in the chiral quark-soliton model, Phys. Rev. C **75,** 055207 (2007).

[28] K. Goeke, J. Grabis, J. Ossmann, M. V. Polyakov, P. Schweitzer, A. Silva, and D. Urbano, Nucleon form-factors of the energy momentum tensor in the chiral quark-soliton model, Phys. Rev. D **75,** 094021 (2007).

[29] M. Wakamatsu, On the D-term of the nucleon generalized parton distributions, Phys. Lett. B **648,** 181 (2007).

[30] M. J. Neubelt, A. Sampino, J. Hudson, K. Tezgin, and P. Schweitzer, Energy momentum tensor and the D term in the bag model, Phys. Rev. D **101,** 034013 (2020).

[31] C. Cebulla, K. Goeke, J. Ossmann, and P. Schweitzer, The nucleon form-factors of the energy momentum tensor in the Skyrme model, Nucl. Phys. **A794,** 87 (2007).

[32] H.-C. Kim, P. Schweitzer, and U. Yakhshiev, Energy-momentum tensor form factors of the nucleon in nuclear matter, Phys. Lett. B **718,** 625 (2012).

[33] I. V. Anikin, Gravitational form factors within light-cone sum rules at leading order, Phys. Rev. D **99,** 094026 (2019).

[34] D. Chakrabarti, C. Mondal, and A. Mukherjee, Gravita-tional form factors and transverse spin sum rule in a light front quark-diquark model in AdS/QCD, Phys. Rev. D **91,** 114026 (2015).

[35] D. Chakrabarti, C. Mondal, A. Mukherjee, S. Nair, and X. Zhao, Gravitational form factors and mechanical properties of proton in a light-front quark-diquark model, Phys. Rev. D **102,** 113011 (2020).

[36] D. Chakrabarti, C. Mondal, A. Mukherjee, S. Nair, and X. Zhao, Proton gravitational form factors in a light-front quark-diquark model, SciPost Phys. Proc. **8,** 113 (2022).

[37] D. Chakrabarti, C. Mondal, and A. Mukherjee, On gravitational form factors and transverse spin sum rule, Few Body Syst. **57,** 437 (2016).

[38] N. Kumar, C. Mondal, and N. Sharma, Gravitational form factors and angular momentum densities in light-front quark-diquark model, Eur. Phys. J. A **53,** 237 (2017).

[39] B. Pasquini, M. V. Polyakov, and M. Vanderhaeghen, Dispersive evaluation of the D-term form factor in deeply virtual Compton scattering, Phys. Lett. B **739,** 133 (2014).

[40] Z. Abidin and C. E. Carlson, Nucleon electromagnetic and gravitational form factors from holography, Phys. Rev. D **79,** 115003 (2009).

[41] C. Mondal, Longitudinal momentum densities in trans-verse plane for nucleons, Eur. Phys. J. C **76,** 74 (2016).

[42] K. A. Mamo and I. Zahed, J/ψ near threshold in holo-graphic QCD: A and D gravitational form factors, Phys. Rev. D **106,** 086004 (2022).

[43] K. A. Mamo and I. Zahed, Nucleon mass radii and distribution: Holographic QCD, lattice QCD and GlueX data, Phys. Rev. D **103,** 094010 (2021).

[44] P. Hagler, J. W. Negele, D. B. Renner, W. Schroers, T. Lippert, and K. Schilling, Moments of nucleon generalized parton distributions in lattice QCD, Phys. Rev. D **68**, 034505 (2003).

[45] M. Gockeler, R. Horsley, D. Pleiter, P. E. L. Rakow, A. Schafer, G. Schierholz, and W. Schroers, Generalized parton distributions from lattice QCD, Phys. Rev. Lett. **92**, 042002 (2004).

[46] J. D. Bratt *et al.*, Nucleon structure from mixed action calculations using $2 + 1$ flavors of asqtad sea and domain wall valence fermions, Phys. Rev. D **82**, 094502 (2010).

[47] P. Hagler *et al.*, Nucleon generalized parton distributions from full lattice QCD, Phys. Rev. D **77**, 094502 (2008).

[48] D. Brommel *et al.*, Moments of generalized parton distributions and quark angular momentum of the nucleon, Proc. Sci. LATTICE2007 (**2007**) 158 [arXiv:0710.1534].

[49] M. Deka *et al.*, Lattice study of quark and glue momenta and angular momenta in the nucleon, Phys. Rev. D **91**, 014505 (2015).

[50] X. Cao, Y. Li, and J. P. Vary, Forces inside a strongly-coupled scalar nucleon, Phys. Rev. D **108**, 056026 (2023).

[51] Y. Hatta, A. Rajan, and K. Tanaka, Quark and gluon contributions to the QCD trace anomaly, J. High Energy Phys. 12 (2018) 008.

[52] K. Tanaka, Three-loop formula for quark and gluon contributions to the QCD trace anomaly, J. High Energy Phys. 01 (2019) 120.

[53] G. F. de Téramond, H. G. Dosch, T. Liu, R. S. Sufian, S. J. Brodsky, and A. Deur, Gluon matter distribution in the proton and pion from extended holographic light-front QCD, Phys. Rev. D **104**, 114005 (2021).

[54] J. More, A. Mukherjee, S. Nair, and S. Saha, Gluon contribution to the mechanical properties of a dressed quark in light-front Hamiltonian QCD, Phys. Rev. D **107**, 116005 (2023).

[55] C. Alexandrou, S. Bacchio, M. Constantinou, J. Finkenrath, K. Hadjiyiannakou, K. Jansen, G. Koutsou, H. Panagopoulos, and G. Spanoudes, Complete flavor decomposition of the spin and momentum fraction of the proton using lattice QCD simulations at physical pion mass, Phys. Rev. D **101**, 094513 (2020).

[56] P. E. Shanahan and W. Detmold, Gluon gravitational form factors of the nucleon and the pion from lattice QCD, Phys. Rev. D **99**, 014511 (2019).

[57] Y.-B. Yang, M. Gong, J. Liang, H.-W. Lin, K.-F. Liu, D. Pefkou, and P. Shanahan, Nonperturbatively renormalized glue momentum fraction at the physical pion mass from lattice QCD, Phys. Rev. D **98**, 074506 (2018).

[58] Y.-B. Yang, J. Liang, Y.-J. Bi, Y. Chen, T. Draper, K.-F. Liu, and Z. Liu, Proton mass decomposition from the QCD energy momentum tensor, Phys. Rev. Lett. **121**, 212001 (2018).

[59] C. Alexandrou, M. Constantinou, K. Hadjiyiannakou, K. Jansen, C. Kallidonis, G. Koutsou, A. Vaquero Avilés-Casco, and C. Wiese, Nucleon spin and momentum decomposition using lattice QCD simulations, Phys. Rev. Lett. **119**, 142002 (2017).

[60] D. A. Pefkou, D. C. Hackett, and P. E. Shanahan, Gluon gravitational structure of hadrons of different spin, Phys. Rev. D **105**, 054509 (2022).

[61] K. A. Mamo and I. Zahed, Diffractive photoproduction of J/ψ and Υ using holographic QCD: Gravitational form factors and GPD of gluons in the proton, Phys. Rev. D **101**, 086003 (2020).

[62] Y. Hatta and D.-L. Yang, Holographic J/ψ production near threshold and the proton mass problem, Phys. Rev. D **98**, 074003 (2018).

[63] R. Boussarie and Y. Hatta, QCD analysis of near-threshold quarkonium leptoproduction at large photon virtualities, Phys. Rev. D **101**, 114004 (2020).

[64] A. Ali *et al.*, First measurement of near-threshold J/ψ exclusive photoproduction off the proton, Phys. Rev. Lett. **123**, 072001 (2019).

[65] M. F. M. Lutz *et al.*, Physics performance report for PANDA: Strong interaction studies with antiprotons, arXiv:0903.3905.

[66] V. Abgaryan *et al.*, Status and initial physics performance studies of the MPD experiment at NICA, Eur. Phys. J. A **58**, 140 (2022).

[67] S. Kumano, J-PARC hadron physics and future possibilities on color transparency, MDPI Phys. **4**, 565 (2022).

[68] J. P. Vary, H. Honkanen, J. Li, P. Maris, S. J. Brodsky, A. Harindranath, G. F. de Teramond, P. Sternberg, E. G. Ng, and C. Yang, Hamiltonian light-front field theory in a basis function approach, Phys. Rev. C **81**, 035205 (2010).

[69] X. Zhao, H. Honkanen, P. Maris, J. P. Vary, and S. J. Brodsky, Electron $g - 2$ in light-front quantization, Phys. Lett. B **737**, 65 (2014).

[70] S. Nair, C. Mondal, X. Zhao, A. Mukherjee, and J. P. Vary, Basis light-front quantization approach to photon, Phys. Lett. B **827**, 137005 (2022).

[71] P. Wiecki, Y. Li, X. Zhao, P. Maris, and J. P. Vary, Basis light-front quantization approach to positronium, Phys. Rev. D **91**, 105009 (2015).

[72] Y. Li, P. Maris, X. Zhao, and J. P. Vary, Heavy quarkonium in a holographic basis, Phys. Lett. B **758**, 118 (2016).

[73] S. Jia and J. P. Vary, Basis light front quantization for the charged light mesons with color singlet Nambu–Jona-Lasinio interactions, Phys. Rev. C **99**, 035206 (2019).

[74] J. Lan, C. Mondal, S. Jia, X. Zhao, and J. P. Vary, Parton distribution functions from a light front Hamiltonian and QCD evolution for light mesons, Phys. Rev. Lett. **122**, 172001 (2019).

[75] J. Lan, C. Mondal, S. Jia, X. Zhao, and J. P. Vary, Pion and kaon parton distribution functions from basis light front quantization and QCD evolution, Phys. Rev. D **101**, 034024 (2020).

[76] S. Tang, Y. Li, P. Maris, and J. P. Vary, B_c mesons and their properties on the light front, Phys. Rev. D **98**, 114038 (2018).

[77] S. Tang, Y. Li, P. Maris, and J. P. Vary, Heavy-light mesons on the light front, Eur. Phys. J. C **80**, 522 (2020).

[78] C. Mondal, S. Xu, J. Lan, X. Zhao, Y. Li, D. Chakrabarti, and J. P. Vary, Proton structure from a light-front Hamiltonian, Phys. Rev. D **102,** 016008 (2020).

[79] S. Xu, C. Mondal, J. Lan, X. Zhao, Y. Li, and J. P. Vary, Nucleon structure from basis light-front quantization, Phys. Rev. D **104,** 094036 (2021).

[80] J. Lan, C. Mondal, M. Li, Y. Li, S. Tang, X. Zhao, and J. P. Vary, Parton distribution functions of heavy mesons on the light front, Phys. Rev. D **102,** 014020 (2020).

[81] W. Qian, S. Jia, Y. Li, and J. P. Vary, Light mesons within the basis light-front quantization framework, Phys. Rev. C **102,** 055207 (2020).

[82] J. Lan, K. Fu, C. Mondal, X. Zhao, and j. P. Vary, Light mesons with one dynamical gluon on the light front, Phys. Lett. B **825,** 136890 (2022).

[83] Z. Zhu, Z. Hu, J. Lan, C. Mondal, X. Zhao, and J. P. Vary, Transverse structure of the pion beyond leading twist with basis light-front quantization, Phys. Lett. B **839,** 137808 (2023).

[84] S. Xu, C. Mondal, X. Zhao, Y. Li, and J. P. Vary, Quark and gluon spin and orbital angular momentum in the proton, Phys. Rev. D **108,** 094002 (2023).

[85] T. Peng, Z. Zhu, S. Xu, X. Liu, C. Mondal, X. Zhao, and J. P. Vary, Basis light-front quantization approach to Λ and Λc and their isospin triplet baryons, Phys. Rev. D **106,** 114040 (2022).

[86] Z. Kuang, K. Serafin, X. Zhao, and J. P. Vary, All-charm tetraquark in front form dynamics, Phys. Rev. D **105,** 094028 (2022).

[87] S. J. Brodsky, G. F. de Teramond, H. G. Dosch, and J. Erlich, Light-front holographic QCD and emerging confinement, Phys. Rep. **584,** 1 (2015).

[88] Z. Hu, S. Xu, C. Mondal, X. Zhao, and J. P. Vary, Transverse momentum structure of proton within the basis light-front quantization framework, Phys. Lett. B **833,** 137360 (2022).

[89] Y. Liu, S. Xu, C. Mondal, X. Zhao, and J. P. Vary, Angular momentum and generalized parton distributions for the proton with basis light-front quantization, Phys. Rev. D **105,** 094018 (2022).

[90] C. Mondal, J. Lan, K. Fu, S. Xu, Z. Hu, X. Zhao, and J. P. Vary, Hadron structure from basis light-front quantization, SciPost Phys. Proc. **10,** 036 (2022).

[91] S. Kaur, S. Xu, C. Mondal, X. Zhao, and J. P. Vary, Spatial imaging of proton via leading-twist GPDs with basis light-front quantization, Phys. Rev. D **109,** 014015 (2024).

[92] Y. Liu, S. Xu, C. Mondal, X. Zhao, and J. P. Vary, Skewed generalized parton distributions of proton from basis light-front quantization, Phys. Lett. B **855,** 138809 (2024).

[93] A. Harindranath, R. Kundu, A. Mukherjee, and J. P. Vary, Sum rule for the twist four longitudinal structure function, Phys. Lett. B **417,** 361 (1998).

[94] X. Ji, X. Xiong, and F. Yuan, Transverse polarization of the nucleon in parton picture, Phys. Lett. B **717,** 214 (2012).

[95] A. Harindranath, R. Kundu, and A. Mukherjee, On transverse spin sum rules, Phys. Lett. B **728,** 63 (2014).

[96] Y. Li and J. P. Vary, Stress inside the pion in holographic light-front QCD, Phys. Rev. D **109,** L051501 (2024).

[97] S. J. Brodsky and G. F. de Teramond, Light-front dynamics and AdS/QCD correspondence: Gravitational form factors of composite hadrons, Phys. Rev. D **78,** 025032 (2008).

[98] S. J. Brodsky, S. Gardner, and D. S. Hwang, Discrete symmetries on the light front and a general relation connecting the nucleon electric dipole and anomalous magnetic moments, Phys. Rev. D **73,** 036007 (2006).

[99] Z. Zhang, Z. Hu, S. Xu, C. Mondal, X. Zhao, and J. P. Vary, Twist-3 generalized parton distribution for the proton from basis light-front quantization, Phys. Rev. D **109,** 034031 (2024).

[100] M. M. Brisudova and S. D. Glazek, Relativistic scattering and bound state properties in a special Hamiltonian model, Phys. Rev. D **50,** 971 (1994).

[101] M. Burkardt, Dynamical vertex mass generation and chiral symmetry breaking on the light front, Phys. Rev. D **58,** 096015 (1998).

[102] M. Burkardt and A. Langnau, Rotational invariance in light cone quantization, Phys. Rev. D **44,** 3857 (1991).

[103] P. Hagler et al., Nucleon generalized parton distributions from full lattice QCD, Phys. Rev. D **77,** 094502 (2008).

[104] Y. L. Dokshitzer, Calculation of the structure functions for deep inelastic scattering and $e + e-$ annihilation by perturbation theory in quantum chromodynamics., Sov. Phys. JETP **46,** 641 (1977), http://www.jetp.ras.ru/cgi-bin/dn/e_046_04_0641.pdf.

[105] V. N. Gribov and L. N. Lipatov, Deep inelastic e p scattering in perturbation theory, Sov. J. Nucl. Phys. **15,** 438 (1972).

[106] G. Altarelli and G. Parisi, Asymptotic freedom in Parton language, Nucl. Phys. **B126,** 298 (1977).

[107] G. P. Salam and J. Rojo, A higher order perturbative parton evolution toolkit (HOPPET), Comput. Phys. Commun. **180,** 120 (2009).

[108] S. J. Brodsky, D. S. Hwang, B.-Q. Ma, and I. Schmidt, Light cone representation of the spin and orbital angular momentum of relativistic composite systems, Nucl. Phys. **B593,** 311 (2001).

[109] D. C. Hackett, D. A. Pefkou, and P. E. Shanahan, Gravitational form factors of the proton from lattice QCD, Phys. Rev. Lett. **132,** 251904 (2024).

[110] M. V. Polyakov, Generalized parton distributions and strong forces inside nucleons and nuclei, Phys. Lett. B **555,** 57 (2003).

[111] H.-Y. Won, H.-C. Kim, and J.-Y. Kim, Mechanical structure of the nucleon and the baryon octet: Twist-2 case, J. High Energy Phys. 05 (2024) 173.

[112] K. Azizi and U. Özdem, Nucleon's energy–momentum tensor form factors in light-cone QCD, Eur. Phys. J. C **80,** 104 (2020).

[113] J.-H. Jung, U. Yakhshiev, H.-C. Kim, and P. Schweitzer, In-medium modified energy-momentum tensor form factors of the nucleon within the framework of a π-ρ-ω soliton model, Phys. Rev. D **89,** 114021 (2014).

[114] H.-Y. Won, J.-Y. Kim, and H.-C. Kim, Gravitational form factors of the baryon octet with flavor SU(3) symmetry breaking, Phys. Rev. D **106,** 114009 (2022).

[115] I. V. Anikin *et al.*, Nucleon and nuclear structure through dilepton production, Acta Phys. Pol. B **49**, 741 (2018).

[116] C. Lorcé, A. Metz, B. Pasquini, and S. Rodini, Energy-momentum tensor in QCD: Nucleon mass decomposition and mechanical equilibrium, J. High Energy Phys. 11 (2021) 121.

[117] A. Freese and G. A. Miller, Forces within hadrons on the light front, Phys. Rev. D **103**, 094023 (2021).

[118] J. Y. Panteleeva and M. V. Polyakov, Forces inside the nucleon on the light front from 3D Breit frame force distributions: Abel tomography case, Phys. Rev. D **104**, 014008 (2021).

[119] J.-Y. Kim and H.-C. Kim, Energy-momentum tensor of the nucleon on the light front: Abel tomography case, Phys. Rev. D **104**, 074019 (2021).